

An overview of the structural correlation of magnetic and electrical properties of Pr₂NiMnO₆ Double perovskite

ABSTRACT

Double perovskites R₂NiMnO₆ (R= Rare earth element) (RNMO) are a significant class of materials owing to their varied tunability of the magnetic and electrical properties with the structural modifications. Pr₂NiMnO₆ (PNMO) is one among the least explored members of this series, which shows spin phonon coupling, magnetocaloric effect and electrochemical performance for various applications such as spintronics, magnetocaloric refrigerant and solid oxide fuel cells. Most of the studies in PNMO is limited to the application domain and focus on the comparative study with different rare earth elements. Detailed structural studies like neutron diffraction are sparse in PNMO samples which will give a perception to the ordering in the compound that strongly depend on the physical and chemical properties. This review article goes through the various aspects of PNMO materials that have been reported till now and showcases the octahedral distortions and corresponding structural changes and the exchange interactions, which in turn correlates with the magnetic and electrical properties. The comparison study of PNMO with other members of the RNMO family and the relevance of PNMO over other members is also tried to showcase through this article. Hope this article provides an insight to the scope of studies in PNMO material for exploring unexposed properties of the materials in the double perovskite family.

Introduction

Multiferroic materials with novel physical properties^{1,2} are technologically useful and offer scopes in understanding rich physics. The perovskite oxide ABO₃ In which A site is 12 coordinated and the B site is octahedrally coordinated. The most interesting class of compounds with A position is occupied by rare earth or alkaline earth ions with large ionic radii and the B position is generally a transition metal (TM) ion or rare earth ion with smaller ionic radii that exhibit various physical properties. It contains corner sharing BO₆ octahedra and the voids are filled by the larger radius A cations. Fractional substitution at different extent at A and B lattice sites can make these compounds rich in variations in tuning the properties. In this the fraction of one type of cation is replaced by another cation. These substitutions are possible in A site alone, B site alone, and both A and B site cations. When these cations are ordered then the structure becomes double perovskite with formula AA'B₂O₆³ A₂B'B''O₆, AA'B'B''O₆⁴. Two types of B cation ordering is possible mainly, that results in a double perovskite structure in a

composition of $AB'_{1/2}B''_{1/2}O_3$ ⁵ or $A_2B'B''O_6$ as the substitution percentage at the B site reaches 50%^{6,7}. The illustration of the $A_2B'B''O_6$ in the rock salt double perovskite structure in which the A cations are surrounded by an alternating network of $B'O_6$ and $B''O_6$ octahedra are depicted in the book, *Perovskite: Crystallography, Chemistry and Catalytic Performance* (Nova Publishers, 2013)¹⁵. Other kinds of double perovskites also occur, such as $AB'_{1/3}B''_{2/3}O_3$ ⁸ $AB'_{1/4}B''_{3/4}O_3$ ⁷. The BO_6 octahedra can expand/contract and tilt for compensating the non-ideal ionic size ratios. Also, electronic instabilities may cause the cations to move from their ideal pseudo cubic positions or the distortions of octahedra can occur. In this double perovskite structure partial doping of other elements and creation of vacancies on any of the lattice sites can be possible. This flexibility enables most of the elements in the periodic table to occupy this perovskite lattice sites^{9,10}. Because of the different electronic arrangements and ionic radii of TM ions, various properties can be studied by modulating the combinations and interactions among the TM ions. In $A_2B'B''O_6$ Perfect ordering of ions in B' and B'' sites is occasional and many physical and chemical properties are interrelated with the extent of ordering. A site can be occupied with A^{1+} (Alkali elements), A^{2+} (Ca, Sr, Ba, Pb, Cd) and A^{3+} (Rare earth elements) cations. $R_2B'B''O_6$ (R = rare earth, Sc, Y) have R^{3+} cation and a combination of B'^{1+}/B''^{5+} , B'^{2+}/B''^{4+} , B'^{3+}/B''^{3+} , cations in the Double perovskite structure⁷. R cation is having coordination number 8. B cations are in octahedral coordination. Because of the large octahedral tilting some of the nearest neighbour anions get out of the first coordination sphere of the R cation. This is the reason behind the reduced coordination number of R is 8 rather than 12. An anion which is more than 3 Å far from A cation of the double perovskites can be considered to be outside the coordination sphere¹¹. The research in area of A site ordering of this family of double perovskites is less compared to the B site ordering. The result of these rare studies of A site ordering is particularly due to the fact that most of the materials with these sorts of ordering needs high pressure synthesis and exist over a very narrow range of temperature¹²⁻¹⁴.

The studies of RNMO where A site is occupied with rare earth and the B site is with Ni and Mn ions is an interesting field of research. Recently the research related to each member of the RNMO family has flourished due to the extensive properties exhibited by the LNMO material. The magnetic and electrical properties in RNMO are structure correlated and in this review paper structural and physical properties and the various applications of double perovskite PNMO so far has been investigated.

Parent compounds Single perovskites PrMnO₃ and PrNiO₃

In Rare-earth Nickelates RNiO₃ the band-structure shows a rich phase diagram, which can change through the parameters such as rare earth ionic radius, Ni–O–Ni bond angle, strain, etc^{16,17}. Strongly correlated systems like rare earth manganites RMnO₃ also exhibit properties such as magnetocaloric effect, colossal magnetoresistance, charge-ordering and many other exciting properties as well^{18–25}. Ni and Mn ions which are Jahn-Teller ions lead to the electronic and magnetic properties in these two perovskite systems.

The parent compounds of PNMO double perovskites are single perovskites PrNiO₃ and PrMnO₃ which are having Orthorhombic *Pbnm* structure with Pr³⁺ occupying the A site and B sites are occupied by Mn³⁺ in PrMnO₃ and Ni³⁺ in PrNiO₃ respectively. PrMnO₃ is an A-type and PrNiO₃ is a G-type antiferromagnetic insulator, whereas Pr₂NiMnO₆ is a ferromagnetic insulator²⁶. In PrMnO₃ the spins are ferromagnetically aligned in the basal plane and antiferromagnetic arrangement of spins in the perpendicular direction with Neel temperature at T_N ≈ 100 K^{27,28}. In RNiO₃ below the characteristic metal–insulator transitions the charge disproportionation of Ni^{3+δ} and Ni^{3-δ} is observed,²⁹ with δ being larger for the heavier lanthanides.³⁰

Ni–O–Ni bond in PrNiO₃ and Mn–O–Mn bond in PrMnO₃ is having p band to d band interaction, which significantly influence physical properties of both compounds. Oxygen annealing is having a great impact on p band and d band overlap³¹. There is a sharp transition of metal (paramagnetic state) at high temperature to insulator (antiferromagnetic state) at lower temperature in PrNiO₃. This metal insulator transition temperature (TMI) is associated with significant change in conductivity³². TMI of PrNiO₃ is the same as the Neel temperature (TN). Hence these properties make PrNiO₃ and PrMnO₃ as perfect materials for exploring the structure correlated magnetic and electrical properties³¹. Many studies have been reported for single perovskite PrMnO₃^{27,33–40} and PrNiO₃^{32,41–44}, A site modified PrMnO₃^{18–25,45–49} and PrNiO₃^{50,51}, B site modified PrMnO₃^{52,53} and PrNiO₃^{32,54} and A and B site modified PrMnO₃^{55–61} and PrNiO₃⁶², theoretical studies on PrMnO₃^{38–40} and PrNiO₃⁴³, structural and optical studies^{27,34–36,41,57} for various applications such as catalysis^{37,40,55} solid oxide fuel cells,^{33,46} Colossal Magnetoresistance,^{23,48} Colossal Dielectric Response⁴⁷, Multiferroicity^{24,42}, Ferroelectricity¹⁹, Ferromagnetism^{18,20}, Antiferromagnetism⁵⁶, Magneto caloric effect^{25,58,60}, Unusual metamagnetism⁵⁹, Thermoelectric property⁶¹, Water oxidation⁴⁴ etc.

Combination of different elements at B'/B'' site with Pr at A site in double perovskite R₂B' B''O₆

The double perovskite structure can be influenced with the B-site cation ordering, bond covalency, ionic radii of cations, electronic instabilities, bonding preferences, oxygen content and synthesis conditions ⁷. As a general rule a disordered arrangement is possible when the oxidation state difference of B' and B'' is less than two (E.g., Pr₂CrFeO₆), whereas, if it differ by greater than two, nearly always leads to an ordered arrangement (E.g., Pr₂LiRuO₆). When the oxidation state difference is two (E.g., Pr₂NiMnO₆), disordered, partially ordered, or fully ordered arrangements occur based on differences in size and/or preference of bonding of the B' and B'' ions ¹¹.

Periodic Table of the Elements

Legend:
■ - A site
■ - B'/B'' site

PrB'B''O₆ double perovskites

1	2											13	14	15	16	17	18		
H	He											B	C	N	O	F	Ne		
3	4											11	12						
Li	Be											Al	Si	P	S	Cl	Ar		
5	6	7	8	9	10	11	12					13	14	15	16	17	18		
Na	Mg	K	Ca	Sc	Ti	V	Cr	Mn	Fe	Co	Ni	Cu	Zn	Ga	Ge	As	Se	Br	Kr
19	20	21	22	23	24	25	26	27	28	29	30	31	32	33	34	35	36	37	38
Rb	Sr	Y	Zr	Nb	Mo	Tc	Ru	Rh	Pd	Ag	Cd	In	Sn	Sb	Te	I	Xe		
39	40	41	42	43	44	45	46	47	48	49	50	51	52	53	54	55	56	57	58
Cs	Ba	Hf	Ta	W	Re	Os	Ir	Pt	Au	Hg	Tl	Pb	Bi	Po	At	Rn			
87	88	89-103	104	105	106	107	108	109	110	111	112	113	114	115	116	117	118		
Fr	Ra	Rf	Db	Sg	Bh	Hs	Mt	Ds	Rg	Cn	Nh	Fl	Mc	Lv	Ts	Og			
23	24	25	26	27	28	29	30	31	32	33	34	35	36	37	38	39	40	41	42
La	Ce	Pr	Nd	Pm	Sm	Eu	Gd	Tb	Dy	Ho	Er	Tm	Yb	Lu					
57	58	59	60	61	62	63	64	65	66	67	68	69	70	71					
89	90	91	92	93	94	95	96	97	98	99	100	101	102	103					
Ac	Th	Pa	U	Np	Pu	Am	Cm	Bk	Cf	Es	Fm	Md	No	Lr					
89	90	91	92	93	94	95	96	97	98	99	100	101	102	103					

Figure 1: The choice of different elements in the B' and B'' sites with Pr at A site in the double perovskite structure.

Double perovskite structure with Pr at A site and different combinations of elements at B' and B'' sites are studied with various groups and those available in literature is tabulated in Table 1. Different elements can occupy the B site in different combinations to form the Pr₂B'B''O₆ double perovskite structure (Fig:2). The periodic arrangement of these ions gives significant effects to the conductivity, thermal expansion behavior and catalytic properties apart from changes in the magnetic and electrical properties ⁶³⁻⁶⁵.

Depending on the element in the B'/ B'' site there are changes in the exchange interaction of these compounds. The charge difference and the size difference are having a significant role in the arrangement of the B cation sublattice. As the charge and size difference among B cations increases, the stability of rock salt arrangement becomes more stable than random arrangement. Anderson *et al.* in 1993 reported that the main criteria for ordering in perovskite compounds are the charge difference, size, electronic configuration of B-cation and the size mismatch between A/B cations ⁶⁶. Depending on the

Summary of all known double perovskite with Pr at A site and different combination of elements at B' and B'' sites		
A site	B' site	B'' Site
Pr	Li	Ir ⁶⁷ , Ru ⁶⁸ , Os ⁶⁹
	Na	Ir ⁷⁰ , Pt, Sn, Ti ⁷¹ , Os ⁷² , Ru ⁷³
	Mn	Rh ⁷⁴ , Ti ⁷⁵ , Co ⁷⁶⁻⁷⁹ , Cr ^{80,81} , Sb ⁸²
	Cu	Sn, Zr ⁸³ , Ir ⁶⁶ , Ti ⁸⁴
	Ni	Pt ⁸⁵ , Ru ⁷¹ , Ir ⁸⁶ , Mn ^{26,87,88} , Zr ⁸⁹
	Co	Pt ⁸⁵ , Ru ⁹⁰
	Zn	Pt ⁸⁵ , Ti ⁹¹ , Zr ⁹²
	Fe	Cr ^{93,94}
	Mg	Ir ^{67,86} , Pt ⁸⁵

superexchange interaction between the B' and B'' cations the material shows ferromagnetic or antiferromagnetic ordering. Also, the presence of different magnetic ions in the lattice sites create various magnetic interactions which leads to the canted spins in the lattice. These canted spins create additional magnetic transitions observed in the thermo magnetization curves. The structural variations and the differences in the exchange interactions of different ions at B' and B'' sites with Pr at A site is tabulated in Table 2.

The relevance of Ni and Mn at B' and B'' site

RNMO materials are a distinct class of double perovskite oxides, in which $e_g^2-O-e_g^0$ electronic interaction leads d electron spins to align ferromagnetically based on the classical Goodenough–Kanamori rules^{95,96}. In $\text{La}_2\text{NiMnO}_6$ (LNMO) a ferromagnetic transition temperature ($T_C = 280$ K) which is near room temperature attracted considerable attention to this class of compounds^{10,97}. Numerous properties have been explored lately in this system such as magnetocapacitance^{10,98} colossal magnetoresistance⁹⁹⁻¹⁰¹, super conductivity^{102,103}, magnetodielectric properties¹⁰, catalytic property¹⁰⁴⁻¹⁰⁶, multiferroicity^{1,2,107,108}. Novel technologically advanced devices like spin filter junctions and multiple state memory elements can be designed with the utilization of the complex physical properties of RNMO materials¹⁰⁹⁻¹¹³. Also, they provide different opportunities to induce multiferroicity and its modulation in oxide systems.

Table 2: structural, exchange interaction and curie temperature of double perovskite with Pr AT a site and different combination of TM at B'/B'' site

Material	Space group	oxidation state	Bond length	Bond angle	β	Curie temperature (Tc)/Neel temperature (TN)	Superexchange interaction
Pr ₂ MgIrO ₆	P2 ₁ /n [a ⁻ a ⁺ b ⁺]	Mg ²⁺ , Ir ⁴⁺	Mg-O =2.058 Ir-O =2.014	150.27	90.006	T _N = 14 K	Antiferromagnetic interaction
Pr ₂ NaRuO ₆	P2 ₁ /n [a ⁻ a ⁺ b ⁺]	Na ⁺ , Ru ⁵⁺	Na-O=2.278 Ru-O=1.954	142.93	90.786	T _N = ~20 K	Antiferromagnetic interaction (spin canted weak ferromagnetism)
Pr ₂ LiIrO ₆	P2 ₁ /n [a ⁻ a ⁺ b ⁺]	Li ⁺ , Ir ⁵⁺	Li-O=2.106 Ir-O = 1.970	149.43	90.222	T _N = ~57 K	Antiferromagnetic interaction
Pr ₂ LiOsO ₆	P2 ₁ /n [a ⁻ a ⁺ b ⁺]	Li ⁺ , Os ⁵⁺	Li-O = 2.113 Os-O = 1.963	148.9	90.407	T _N =35 K	Antiferromagnetic interaction
Pr ₂ LiRuO ₆	P2 ₁ /n [a ⁻ a ⁺ b ⁺]	Li ⁺ , Ru ⁵⁺	Li-O= 2.103 Ru-O= 1.950	150	90.285	T _N =31 K	Antiferromagnetic interaction
Pr ₂ NiIrO ₆	P2 ₁ /n [a ⁻ a ⁺ b ⁺]	Ni ²⁺ , Ir ⁴⁺	Ni-O = 2.063 Ir-O = 2.012	149.4	90.005	T _N = 105k	Antiferromagnetic interaction (spin canted weak ferromagnetism)
Pr ₂ NaIrO ₆	P2 ₁ /n	Na ⁺ , Ir ⁵⁺	Na-O = 2.282 Ir-O = 1.972	142.37	90.793	-	absent
Pr ₂ CuSnO ₆	P2 ₁ /m	Cu ²⁺ , Sn ⁴⁺	Cu-O = 2.086	156	91.716	T _{N1} =220 K T _{N2} = below 40 K	Antiferromagnetic interaction (spin canted weak ferromagnetism)
Pr ₂ FeCrO ₆	R3c	Fe ³⁺ , Cr ³⁺	-	-	-	T _C = 562 K	Ferromagnetism
Pr ₂ FeCrO ₆	Pbnm [a ⁺ a ⁺ b ⁻]	Fe ³⁺ , Cr ³⁺	Fe/Cr -O= 1.753	159.77	-	T _C = 240 K	Ferromagnetism (spin canted weak antiferromagnetism)
Pr ₂ CrMnO ₆	pbnm	Cr ²⁺ , Mn ⁴⁺	-	159.73	90	T _C = 93.74	Ferromagnetic interaction
Pr ₂ CoMnO ₆	P2 ₁ /n	Co ²⁺ , Mn ⁴⁺	-	-	-	T _C =173 K	Ferromagnetic interaction
Pr ₂ NaOsO ₆	P2 ₁ /n [a ⁻ a ⁺ b ⁺]	Na ⁺ , Os ⁵⁺	Na-O = 2.291 Os-O = 1.967	-	90.854	T _{N1} =20 K T _{N2} =10 K	Antiferromagnetic interaction
Pr ₂ CoRuO ₆	P2 ₁ /n	Co ²⁺ , Ru ⁴⁺	Ru/Co-O= 2.046	146.53	90.005	No magnetic studies	
PrMn _{1/2} Rh _{1/2} O ₃	pbnm	Mn ³⁺ , Rh ³⁺	Mn/Rh-O=2.03	150.33		No magnetic studies	
Pr ₂ ZnTiO ₆	P2 ₁ /n [a ⁺ b ⁺ b ⁻]	Zn ²⁺ , Ti ⁴⁺	Zn-O=2.049 Ti-O=1.955	152.71	90.264	No magnetic studies	
Pr ₂ NiZrO ₆	P2 ₁ /n	Ni ²⁺ , Zr ⁴⁺	Ni-O=1.926 Zr-O=2.267	145	90.059	No magnetic studies	

In the double perovskite $A_2B'B''O_6$ shows a wealth of structural variations due to the presence of three cations to influence the magnetism. There are various possibilities for the occupancy of magnetic cation only at B' site (nonmagnetic ions at B'' and A site), only at A site, only at B'' site, both B' and B'' sites, and finally, the A, B' and B'' sites. For choice of A site cation large ionic radii with magnetic property is needed. There is a great selection of trivalent cations in trivalent lanthanides as ideal candidates to take the role of A site cations. After the selection of lanthanides (Ln) for A site then the compound is $Ln_2B'B''O_6$. In this compound the sum of the B' and B'' oxidation states are limited to +6 (+1/+5, + 2/+4, and +3/+3). When the number of magnetic ions increases the magnetic behaviour of the double perovskite structure becomes complex⁸⁶. In the lanthanide series La^{3+} is a nonmagnetic ion, Pr^{3+} is the largest magnetic ion in the lanthanide series after Ce^{3+} . Moreover, from the viewpoint of magnetism, when the nonmagnetic La ion is replaced with the magnetic Pr ion the various magnetic interactions arise will lead to another dimension of the application of these compounds with richer phase diagrams.

Once the settlement of Pr^{3+} in the A site, next is the choice of elements to B'/B'' sites. The B site ordering is mainly influenced by the charge difference of B' and B'' cations (ΔZ_B) and the size difference of these ions (Δr_B). For $\Delta Z_B > 2$ leads to highly ordered double perovskite structure, whereas $\Delta Z_B < 2$ leads to disordered samples⁷. In the case of Δr_B , the larger the size difference most probable is the ordering. Most interesting class of compounds are $\Delta Z_B = 2$, where order-disorder phenomena are observed. Here a wide range of partial ordering is taking place. Also, for a wide range of size differences both ordered and disordered states are observed, but for small Δr_B disordered states are most favourable. The ordering of B'/ B'' octahedra will be favourable if the size difference is greater than 0.1 Å and charge difference is two or greater than two⁹¹. RNMO family exhibit highly ordered structure with magnetic TM cations Ni^{2+} and Mn^{4+} having a charge difference of 2 and size difference $\Delta r_B = 0.13-0.16$ Å. Also, the ferromagnetic superexchange interaction between these cations also increases the criteria of selecting Ni^{2+} and Mn^{4+} to the B'/B'' sites. For compounds having $\Delta Z_B = 2$ other factors which influence the ordering are synthesis conditions. The annealing temperature and the synthesise pressure will influence the ordering. Another weak effect is the smaller the A site cation larger the B site ordering. This is because smaller A site cations bring the B' and B'' cations closer, which increases the repulsion between them. That leads to the increase in Madelung energy of ordering. Finally, oxygen vacancies also influence the ordering. The compounds with oxygen vacancies are of lesser B site cation order than oxygen stoichiometric

compounds¹¹⁴. In RNMO the ordering of B sites can be done with Ni³⁺/Mn³⁺ or Ni²⁺/Mn⁴⁺. The rock-salt ordering between Ni³⁺ and Mn³⁺ would be derived from the Jahn–Teller character of Mn³⁺, while Ni²⁺/Mn⁴⁺ order would be due to charge ordering. The studies with NMR and XAS^{115–117} show the actual valence states are Ni²⁺ and Mn⁴⁺. The charge ordering of these ions leads to the attractive physical properties of these double perovskites.

Apart from the extensively studied LNMO, studies of other rare earth RNMO oxides are comparatively scarce^{118–122}. Extensive research is carried out for decades for LNMO in the areas of A site doped^{123–125}, B site doped^{126–128}, A and B site doped¹²⁹ and theoretical studies^{130,131} for various technological applications¹³². Because of these multiple properties Researchers are curious about the modulation of these exciting properties with the change of rare earth element. Hence the studies are extended to other members of the RNMO family as well. Even though there are many similarities and regular trends in the physical properties shown by the members of RNMO family there are many differences in the properties which are related with the particular rare earth ion and the coupling between rare earth ion and the Ni–Mn system. These differences can be realized only by exploring each member of the RNMO family through extensive research and correlation studies. The individual studies on different members of the RNMO family also started to explore the physical properties of this distinct group of compounds. Apart from LNMO and PNMO other rare earth (Lanthanides (La to Lu) and Scandium, Yttrium) double perovskites Ce₂NiMnO₆¹³³, Nd₂NiMnO₆ (NNMO)^{134,135}, Pm₂NiMnO₆, Sm₂NiMnO₆ (SNMO)^{136–138}, Eu₂NiMnO₆ (ENMO)^{139–141}, Gd₂NiMnO₆ (GNMO)^{142–144}, Tb₂NiMnO₆ (TNMO)^{145,146}, Dy₂NiMnO₆ (DNMO)^{147–151}, Ho₂NiMnO₆ (HNMO)^{152,153}, Er₂NiMnO₆ (ENMO)^{153,154}, Tm₂NiMnO₆ (TNMO)¹⁵⁵, Yb₂NiMnO₆ (YNMO)¹⁰⁸, Lu₂NiMnO₆ (LNMO)^{156–159}, Sc₂NiMnO₆¹⁶⁰, Y₂NiMnO₆^{161–163} are also now on the path of research.

Due to the comparable size of Mn⁴⁺ and Ni²⁺, the charge difference of 2, which helps to tune ordering of B'/B'' site cations, covalent nature of bonds and superexchange interactions in the compound. TM ions Ni and Mn exhibit a paramount role for influencing the various characteristics exhibited by RNMO double perovskites. Hence Ni/Mn combination at B'/B''-site in R₂B'B''O₆ double perovskite structure brings exciting magnetic and electrical interactions resulting in the formation of new phase or lead to entirely different behaviours. In single perovskite PrNiO₃ and PrMnO₃ the interactions Ni-Ni and Mn-Mn are antiferromagnetic in nature, while oxide systems having both Mn and Ni ions like RNMO there may be the possibility of competition between different magnetic phases³¹.

In PNMO Ni^{2+} and Mn^{4+} occupy the B' and B'' site in an alternate octahedral site, where the charge difference is 2. Blasse *et al.* ¹⁶⁴ explored the magnetic properties of perovskite $\text{La}_2\text{MeMnO}_6$ (Me = Mg, Co, Ni, Cu), where Me has +2 oxidation state and Mn is in +4 state. The magnetic interactions between paramagnetic ions can be ferromagnetic or antiferromagnetic in non-metallic oxides. Goodenough ⁹⁶ and Kanamori ⁹⁵ rules have introduced a set of semiempirical rules to realise these magnetic interactions. The sign of these interactions had been determined earlier by Jonker ¹⁶⁵. The 180° (the lines connecting the interacting cations to the intervening anion make an angle 180°) Me^{2+} - O - Mn^{4+} magnetic interaction through oxygen ions seem to be positive. PNMO double perovskite structured material reported magneto-dielectric, magnetocaloric, spin phonon coupling and electrochemical performance so far, for applications in the field of spintronics ^{88,166,167}, magnetic refrigeration ^{88,152}, Solid oxide fuel cells ^{168,169} etc.

Superexchange interaction in RNMO

Super exchange interaction is derived from the second order perturbation theory. This interaction happens between two magnetic ions mediated through a nonmagnetic ion such as oxygen. This magnetic interaction strongly depends on the Metal – oxygen - metal bond angle. The magnetic interaction through super exchange was introduced by Goodenough ⁹⁶[12]. Tiana *et al.* ¹⁷⁰ pictured in figure:2 about how these super exchange interactions induce ferromagnetism or anti-ferromagnetism in a material. This ferro/anti-ferromagnetism is governed by the Pauli's exclusion principle. Hence in PNMO Mn^{4+} and Ni^{2+} magnetic cations interact via nonmagnetic O^{2-} anions through Mn-O-Ni bond. Since the tilting of MnO_6 and NiO_6 octahedra will reduce the Mn-O-Ni bond angle which will affect this superexchange interaction. Mn^{4+} and Ni^{2+} is in $3d^8$ and $3d^3$ configurations. The oxygen octahedral environment around Ni and Mn ions splits the d levels in t_{2g} and e_g states. The crystal field splitting and the spin splitting are to different extent for Ni and Mn ions. For Mn site the crystal field splitting is smaller, while at Ni site crystal field splitting is larger in comparison with the spin splitting in both ions. This leaves Ni t_{2g} states to be completely filled, Ni e_g states and Mn t_{2g} states being half-filled with Mn e_g states being empty. Super exchange processes between Ni- e_g state and Mn- t_{2g} exhibit anti ferromagnetism. However, Ni- e_g and Mn- e_g states show ferromagnetism based on Hund's rule coupling J_H . Das *et al.* ¹⁷¹ in figure:6 illustrate AFM and FM super exchange paths between Ni- e_g spin ($S = 1$) and Mn- t_{2g} spin ($S = 3/2$) and Ni- e_g spin ($S = 1$) and empty Mn- e_g . The net magnetic interaction $J_{\text{Ni-Mn}}$ is expressed by considering the contributions,

in terms of hopping interaction between Ni- e_g and Mn- e_g (t_{e-e}), Ni- e_g and Mn- t_{2g} hopping interaction (t_{t-e}), separation in energy levels of Ni- e_g – Mn- e_g (Δ_{e-e}) and Ni- e_g – Mn- t_{2g} (Δ_{t-e}), the choice of U and J_H values. The tilting of the NiO₆ and MnO₆ octahedra makes t_{t-e} non-zero, resulting in the variation of Ni–O–Mn angle, from 180°. Electron hopping in e_g - e_g orbital is larger than e_g - t_{2g} . Also, the states of Ni- e_g and Mn- t_{2g} lie closer in energy than Ni- e_g Mn- e_g .

Previous theoretical studies on LNMO demonstrated^{171–173} both t_{2g} and e_g states in the majority spin channel were filled for Ni ions in the d^8 state ($S = 1$) spin configuration, and only the t_{2g} states were occupied in the minority spin channel. Whereas, for the Mn⁴⁺ in d^3 configuration ($S = 3/2$), only the t_{2g} states were fully occupied in the majority spin channel, and both the t_{2g} and e_g states remained empty in the minority spin channel. Only the states with same symmetry and spin are allowed to interact in the superexchange interaction. Interactions between the Ni e_g and Mn e_g symmetries, (filled Ni e_g states and the empty Mn e_g states in majority spin channel) and those between the Ni t_{2g} and Mn t_{2g} symmetries (filled Ni t_{2g} states and the empty Mn t_{2g} states in minority spin channel) leads to ferromagnetic interaction according to Goodenough–Kanamori rules.

Comparison of PNMO with other members of the RNMO family (R = La to Lu (Lanthanides), Ce, Sc, Y) family

In $R_2B'B''O_6$ three cation orderings are possible. (1) The random arrangement of B' and B'' cations lead to $R_2B'_{1/2}B''_{1/2}O_3$. This disordered perovskite sample displays an orthorhombic symmetry with the space group of *Pbnm* at room temperature; (2) Ordered arrangement of B' and B'' cations resulting in a double perovskite $R_2B'B''O_6$. This sample crystallizes in monoclinic symmetry (*P2₁/n*) at room temperature; (3) Many systems, mixed cation ordering exists¹⁷⁴. The B'/B'' cation ordering extends to a few unit cells or domains. Also, all of these three phases are thermodynamically stable¹⁷⁵.

Periodic Table of the Elements
RNMO double perovskite

■ A Site
■ B' and B'' sites

The periodic table shows elements from Hydrogen (H) to Oganesson (Og). Elements La through Lu, Sc, and Y are highlighted in green, indicating they are suitable for the A-site of RNMO double perovskites. Elements Mn, Ni, and Cu are highlighted in blue, indicating they are suitable for the B' and B'' sites.

Figure 2: The choice of different rare earth element in the A site of RNMO double

In the A site of RNMO the trivalent rare earth ions Lanthanides (La to Lu) and Sc and Y can occupy (Fig:5). Decrement in the rare earth ionic radius ($r_{R^{3+}}$) in RNMO leads to the decrease in the unit cell volume. The lattice parameters a and c decrease while the b parameter more or less remains constant^{121,122,176} with decrease in $r_{R^{3+}}$. Also, the value $c/\sqrt{2}$ lies between a and b . The primary force of distortions in this perovskite steric arises due to the reduction in the size of R^{3+} cation.¹⁵⁵ The R-O distances decrease as the size of rare earth decreases. Mn/Ni-O bond lengths increase as the value of $r_{R^{3+}}$ decreases^{121,122}. Whereas the average Ni/Mn-O bond lengths do not have significant variation with the $r_{R^{3+}}$ ^{122,155}. While the Ni-O-Mn bond angle decreases as R^{3+} radius decreases (Table3). In a study of the comparison with the different RNMO compounds a difference concerning $\langle Ni-O \rangle$ and $\langle Mn-O \rangle$ bond lengths have observed. Smaller R cation occupancy to the A site introduced $\langle Ni-O \rangle$ distances are substantially higher whereas $\langle Mn-O \rangle$ distances are smaller.¹⁵⁵ This indicates the charge difference between Ni and Mn is large. Also, this would seem that the charge disproportionation between Ni^{2+} and Mn^{4+} stabilized more effectively with the rare earths having smaller ionic radii.¹⁵⁵ The tilting of the octahedra along the c axis results in the displaced oxygen atom to occupy in between the octahedra. Though octahedral distortions are small, there is a significant variation in the tilting angle of octahedra as $r_{R^{3+}}$ decreases.

Stability and distortion of perovskite crystal structure can be expressed by Goldschmidt tolerance factor (t) as;

$$t = \frac{r_R + r_O}{\sqrt{2} \left[\frac{r_{Ni} + r_{Mn}}{2} + r_O \right]}$$

r_R , r_O , r_{Ni} , and r_{Mn} indicates the effective ionic radii of rare earth, oxygen, Ni, and Mn ions correspondingly¹⁷⁷. For $t < 1$ the A cation radius is less than ideal A site cation and the tilting

of BO₆ octahedra and/or the change of bond length compensate for the size mismatch of this double perovskite structure. For $t > 1$ A site cation is very large and the size mismatch cannot be overcome by the octahedral tilting. For that type of compounds various hexagonal structures are formed rather than perovskite structure⁷. For the trivalent rare earth ions, the ionic radii is smaller than the ideal value of the A site cations which leads to condition $t < 1$ and exhibit octahedral tilting. The value of tolerance factor decreases steadily with decrement in rare earth ionic radii which is interrelated with the electronic and magnetic properties^{120,121}.

The distinct decrement of Rare earth ion radius leads to the reduction in the Ni–O–Mn angle, which determines various characteristics of RMO₃ perovskite oxides¹⁷⁸ as well as RNMO double perovskites¹⁷⁹. In RNMO as the rare earth ionic radius decreases the magnetic and electrical properties changes due to the alteration of superexchange interaction, which is closely related with Ni-O-Mn bond angle. There is a subsequent decrease in T_c as the value of $r_{R^{3+}}$ decreases from La to Lu. Asai *et al.*¹⁷⁹ in a study of RE_{0.5}Me_{0.5}MnO₃ (RE = Rare earth element, Me = Co, Ni) found that T_c of this system completely determined by superexchange interaction between Mn⁴⁺ and Me²⁺ as

$$T_c = \frac{2ZJ_{Me-Mn}\sqrt{S_{Me}(S_{Me} + 1)S_{Mn}(S_{Mn} + 1)}}{3K_B}$$

Where J is the super exchange integral, S represents the spins of ions and Z is the distance between Me²⁺ and O²⁻ ions.

From this relation it is clear that the decrement of T_c in this type of perovskite system is not because of the magnetic interaction of rare earth ions. A geometrical factor, super exchange Ni - O - Mn bond angle is playing a major role in the value of T_c. This superexchange angle depends on the kind of rare earth element in the double perovskite. Hence the decrease of the critical temperature of PNMO compared to LNMO is due to the decrease in the super exchange <Ni - O - Mn> angle from 180°^{121,176}.

The variation of T_c is related with the tilting angle (ϕ) of octahedron. There is linear relationship between T_c and $\cos^2\phi$. Where ϕ is determined from the bond angle as $180 - \langle Ni-O-Mn \rangle / 2$ ¹⁷⁹. There is a better correlation between T_c and R³⁺ radius¹⁸⁰ than with ϕ alone. From ⁵⁵Mn NMR experiments, Asai *et al.*¹⁸¹ have shown that for the RNMO oxides a decrease of covalency of Ni–O and Mn–O bonds is observed when R goes from La to Lu. T_c is controlled not only by the angle ϕ but also by the variation of covalency/ionicity of the Ni–O and Mn–O bonds. R³⁺ radius seems to reflect both these effects and hence provides a better

correlation for the T_C ¹²². In addition to this tilting of octahedra, the decrease of covalency of Ni/Mn-O bonds is also having a significant role in the reduction in the transition temperature as the size of the rare earth decreases. This is explained in one of the earliest studies using NMR hyperfine magnetic field ¹⁸¹.

There is a canted spin arrangement of Ni^{2+} and Mn^{4+} within the ferromagnetic arrangement of RNMO with R ions having lower ionic radii (R= Tb, Ho, Er, Tm). Which gives rise to a net ferrimagnetic arrangement ¹⁵⁵. By Goodenough– Kanamori rules the 180° superexchange interaction Ni^{2+} -O- Mn^{4+} path the sign of the interaction of Ni e_g and Mn e_g ferromagnetic interaction changes to antiferromagnetic as the angle becomes closer to 90° ⁹⁵. The angle decreases as the rare earth ion radii decreases in RNMO. Along with the decrease in angle the evolution of interaction from ferro to antiferromagnetic state makes an intermediate state for these compounds. Also, the magnetic superexchange interactions between perfectly parallel or antiparallel spins are stronger than between spins with different directions. Hence the presence of a major ferromagnetic phase with magnetic frustrations within it leads to a glassy state.

The various physical properties of RNMO materials, like the band gap, saturation magnetization, Curie point (T_C), changes noticeably in different reports ^{121,122,182}. The probable mechanism that leads to magnetism in these materials drew diverse conclusions. various synthesis routes that affect the level of the antisite defect at the Ni/Mn sites and the crystallographic structures may be one of the reasons for these differences in properties. variations in the local atomic structure about the Ni and Mn ions is also having an important role in determining the various physical properties ^{183,184}.

Modifications on the crystal structure that induce changes in magnetic interactions can be done through replacing the A site with different rare earth ions. There are reports like magnetic order of RNMO samples would change from ferromagnetic to E^* -type antiferromagnetic for R = La, Sm to R=Y respectively using DFT calculations. The E^* -type magnetic structure ($\uparrow\uparrow\downarrow\downarrow$) allows a ferroelectric polarization to happen, resulting in multiferroicity ¹³⁰. However, the magnetic measurements show a definite ferromagnetic character of YNMO with specific T_C . It is reported that E^* -type ($\uparrow\uparrow\downarrow\downarrow$) spin arrangements in YNMO exist only at zero magnetic field and this AFM arrangement can be destroyed with application of magnetic field. ¹⁸⁵ This is the reason behind the proposed AFM arrangement is not exhibited by YNMO samples. ¹⁶² The existence of antiferromagnetic interactions on Tb_2NiMnO_6 , Nd_2NiMnO_6 , Sm_2NiMnO_6 , Pr_2NiMnO_6 is possible in the studies carried out in these material ^{186,187}. As expressed by figure:1 by Zhao et al. ¹²¹ the experimentally determined correlation of the rare earth ionic radius with (a) β and

tolerance factor (b) Ni-O-Mn angle (c) Bandgap and Curie temperature (d) Ni/Mn-Bond length are helpful for understanding the correlation of structure and physical properties.

According to the comparison table of RNMO (table 3) there is a presence of secondary magnetic transitions in some samples. In some of the reports these secondary transitions are absent in the same samples. This second transition at lower temperature arises due to the AFM interaction of the antisite defects. Ni-O-Ni and Mn-O-Mn interactions are antiferromagnetic in nature. These weak AFM interactions will lead to the secondary transition at lower temperature. Also, there is a magnetic anomaly observed at very low temperature in the magnetisation curves. For Nd, Sm there is a downturn in FC magnetisation, while for Gd, Tb, Dy, Ho an upturn is observed^{122,188}. There are reports which claim low temperature anomalies of RNMO samples^{121,177}. There are various explanations for this magnetic anomaly and these are still in debate. There are reports which claim this anomaly is due to the antiferromagnetic coupling of the Nd, Sm spins to the Ni/Mn sublattice and the ferromagnetic coupling between Gd, Tb, Dy spins with Ni/Mn sublattice. The magnetic moment of these rare earths is significant only at lower temperature and the moment will follow Hund's rule depending on the less than half filled (Nd, Sm) or more than half filled (Gd, Tb, Dy) conditions. The spin-orbit coupling of rare earth and the Ni/Mn sublattice will lead to this low temperature variation in magnetisation¹⁸⁸. Another claim for this anomaly is that there is no role for the R and Ni/Mn sublattice in these effects. This downturn is observed for RNMO systems irrespective of whether the R ion is magnetic or not. Because this anomaly is observed for YNMO samples where Y³⁺ is a nonmagnetic ion. In such systems this low temperature magnetic anomaly is explained in terms of the random FM and AFM interactions that arise due to the variable oxidation state of Ni and Mn. The random AFM interactions Ni³⁺/Mn³⁺ - O - Ni³⁺/Mn³⁺ and FM interaction Ni²⁺ - O - Mn⁴⁺ along with crystallographic disorder leads to this low temperature anomaly and the glassy state of these oxides¹⁷⁷. Another possibility arises due to the antiphase AFM domains resulting from spatial distribution of Ni²⁺/Mn⁴⁺ ordered domains and the out-of-phase ordering¹⁸⁹.

Table 3 : Structural and magnetic properties of RNMO (Lanthanides,Y) with space group $P2_1/n$								
Double perovskite	Ionic radii (Å)	Space group	Bond length (Å)	Bond angle (°)	β (°)	Magnetic transition temperature (K)	Exchange interaction	
$\text{La}_2\text{NiMnO}_6$ 10,121,190	1.16	$P2_1/n$	Ni-O = 1.97 – 2.02 Mn-O = 1.917- 1.96	160.7- 164.3	89.82- 90.01	T_C - 273,240,280, 266 T_C' - 160,138,102	Ferromagnetic interaction (T_C) Antiferromagnetic interaction at antisite defects/antiphase boundaries (T_C) Anomaly in magnetisation curve (Downturn in magnetisation for Nd, Sm and Upturn in magnetisation Gd, Tb, Dy) (T_2)	
$\text{Ce}_2\text{NiMnO}_6$ ¹³³	1.143		-	-	-	-		
$\text{Nd}_2\text{NiMnO}_6$ 121,122,135,152,174,187,191	1.11	$P2_1/n$	Ni-O = 2.04 Mn-O = 1.915	155-158	90.02 - 90.05	T_C =191- 200 T_C' = ~ 100 T_2 = < 50		
$\text{Pm}_2\text{NiMnO}_6$	1.09		All of its isotopes are radioactive					
$\text{Sm}_2\text{NiMnO}_6$ 136–138,167,167,182,186	1.08	$P2_1/n$	Ni-O = 2.01-2.08 Mn-O = 1.88-1.93	151-154	89.8 - 90.06	T_C -141 – 165 T_C' - 67 T_2 = < 20		
$\text{Eu}_2\text{NiMnO}_6$ 140,141,177	1.066	$P2_1/n$	Ni-O = 1.88-2.01 Mn-O = 1.99-1.96	148.4 - 151.32	90.01- 90.07	T_C -145 T_2 - 6		
$\text{Gd}_2\text{NiMnO}_6$ 122,177,188,192,193	1.05	$P2_1/n$	Ni-O = 2.070-2.19 Mn-O = 1.895-2.03	148.6 - 152.20	90.13 - 90.19	T_C -128,130,132, 134,125 T_2 -20,40,33		
$\text{Tb}_2\text{NiMnO}_6$ 122,146,155,167,188	1.04	$P2_1/n$	Ni-O = 1.99-2.04 Mn-O = 1.907-1.99	140 - 149.5	89.79 - 90.14	T_C -111,110,113 T_2 -12K,15,20,15		
$\text{Dy}_2\text{NiMnO}_6$ ^{140,150,151,153,177,188}	1.027	$P2_1/n$	Ni-O =1.95-2.034 Mn-O = 21.91- 1.924	146.92- 148.5	90.23 - 90.25	T_C -93,105,95,101, 97,95,100 T' -21,6,20,50		
$\text{Ho}_2\text{NiMnO}_6$ ^{121,122,153,186,194}	1.015	$P2_1/n$	Ni-O= 1.99-2.04 Mn-O=1.91-1.99	145.6 146.3	89.72 - 90.21	T_C -82,79,86,93,85		
$\text{Er}_2\text{NiMnO}_6$ ^{153,155}	1.004	$P2_1/n$	Ni-O = 2.04 Mn-O = 1.91	145.33	90.22	T_C - 84,74		
$\text{Tm}_2\text{NiMnO}_6$ ¹⁵⁵	0.994	$P2_1/n$	Ni-O = 2.044 Mn-O = 1.915	144.16	90.29	T_C - 62		
$\text{Yb}_2\text{NiMnO}_6$ ¹⁰⁸	0.985	$Pnma$	Ni/Mn -o = 1.96	-	-	T_C > 350		
$\text{Lu}_2\text{NiMnO}_6$ 156,157,159	0.977	$P2_1/n$	Ni-O = 1.95 Mn-O = 1.99	142.5- 145.5	90.32 - 90.69	T_C - 45,40 T_C' -20		
Y_2NiMnO_6 122,145,162,177,195	1.02	$P2_1/n$	Ni-O = 2.018 Mn-O = 1.938	145.95 147.18	89.74, 90.141	T_C -79,81 T' - 10		

Valence state of cations are R^{3+} , Ni^{2+} and Mn^{4+} (small amounts of Ni^{3+} and Mn^{3+} is also seen in XPS analysis of some reports).
 T_C - the ferromagnetic curie temperature,
 T_C' -The secondary transition due to antisite disorders
 T' - the magnetic anomaly at low temperature

Structural Properties of PNMO

PNMO double perovskite, which is a less explored member of the RNMO series, in which Mn and Ni are arranged in alternatively to produce rock salt type arrangement. Pr^{3+} (ionic radii $\sim 0.99 \text{ \AA}$) occupies the A site and Mn^{4+} ($\sim 0.53 \text{ \AA}$), Ni^{2+} ($\sim 0.69 \text{ \AA}$) in alternate octahedral B' and B'' lattice sites in $\text{A}_2\text{B}'\text{B}''\text{O}_6$. It exhibits two types of crystal structure based on the Ni and Mn crystallographic site occupancies. First one is the orthorhombic crystal structure with the random arrangement of Ni and Mn. Second one is the monoclinic structure with Ni and Mn cations in alternating octahedral arrangement (Fig:7) ^{122,155,182} with lattice parameters $a \approx b \approx \sqrt{2}a_p$ ^{66,196}. Mn and Ni ions occupy the same Wycoff position $2b$ in the orthorhombic $Pnma$ structure. In PNMO according to the following reaction, $\text{Ni}^{3+} + \text{Mn}^{3+} \rightleftharpoons \text{Ni}^{2+} + \text{Mn}^{4+}$ charge disproportionation leads to the formation of Mn^{4+} and Ni^{2+} ^{97,197}.

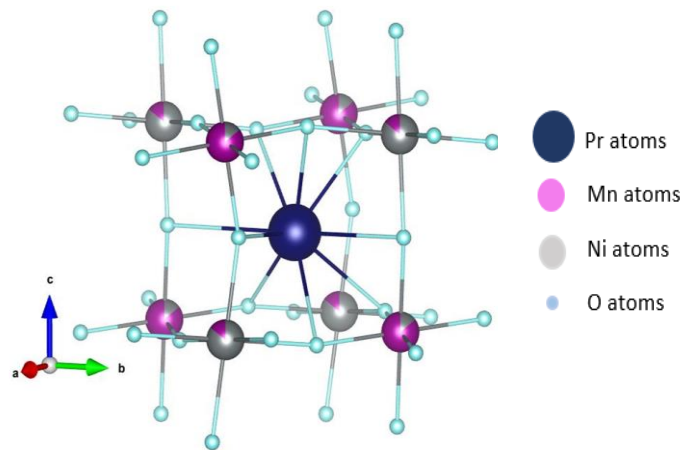


Figure 3: Perovskite Unit of PNMO

Various synthesize routes have been reported for PNMO material ^{4,26,31,87,88,120–122,152,166,168,176,181,198–200} such as modified nitrate decomposition route ¹²⁰, glycine nitrate method ¹⁹⁸, sol gel process ^{4,121}, Hydrothermal route²⁰⁰, Pechini method ¹⁶⁷, solid state reaction route ^{26,88,122,152,166,168,199}. The ordering of Ni, Mn also depends on synthesis technique ¹⁹⁷. The cation composition and deviation of oxidation states of Ni^{2+} and Mn^{4+} are affected by the oxygen partial pressure of annealing atmosphere and they in turn govern their magnetic properties. The influences of these parameters on the dielectric properties have also been reported in the literature ^{201,202}

Determination of the pattern of B cations ordering is difficult with XRD analysis due to the resemblance in scattering factors. Neutron diffraction is an important tool to ensure the ordering of B'/B" sites. Rietveld refinement of XRD data well fitted with the single phase of PNMO with monoclinic $P2_1/n$ space group^{26,88,120–122,152,167,168,198–200}. Rietveld refinement of the XRD patterns of PNMO at room temperature is shown in figure :1 by Lekshmi *et al.*¹⁶⁷

Bull *et al.*¹²⁰ indexed the peaks corresponding to an orthorhombic unit cell $Pnma$. While due to B cation ordering less symmetric monoclinic $P2_1/n$ is observed through the neutron diffraction analysis. In the monoclinic symmetry Ni^{2+} and Mn^{4+} ions occupy $2c$ (0,1/2,0) and $2d$ (1/2,0,0) sites respectively and Pr^{3+} and O^{2-} ions are occupy at general lattice sites $4e$ (x, y, z)^{203,204}. The structural parameters obtained from XRD are tabulated in Table 2.

Reference	Lattice parameters	Bond length	Bond angle Ni-O-Mn
Zhang <i>et al.</i> ²¹	a = 5.4339 Å, b = 5.4451Å, c = 7.6910Å β = 89.497 ⁰ , V = 227.55	Mn-O=1.892Å Ni-O= 2.166 Å	158.014 ⁰
Truong <i>et al.</i> ²²	a = 5.54 Å, b = 5.50 Å c = 7.70 Å	Mn-O=1.928Å Ni-O = 2.029Å	158.6 ⁰
Booth <i>et al.</i> ¹⁶	a = 5.4453 Å, b = 5.4701Å, c = 7.696Å, β = 90.030 ⁰ , V = 229.257	Mn-O=1.928Å Ni-O= 2.029 Å	158.6 ⁰
Balasubramanyam <i>et al.</i> ²⁰	a =5.4672Å b = 5.5362Å c= 7.7336 Å β = 89.88 ⁰ , V = 234.07	Mn-O=1.93Å Ni-O= 2.04 Å	-
Nazir <i>et al.</i> ¹⁵	a =5.44 Å b = 5.47 Å c= 7.69 Å β = 90.01 ⁰ , V= 228.5	Ni/Mn -O =1.97 Å	157 ⁰
NeenuLakshmi <i>et al.</i> ³⁰	a = 5.4455, b= 5.4692, c = 7.6964, β =90.01 ⁰ , V = 229.22	-	155.6 ⁰

From the table 2, it is obvious that there is a structural change in the PNMO monoclinic angle β from 90⁰ which is due to the lower ionic radius of Pr^{3+} which in turn cause octahedral tilting for attaining stability. With maintaining the corner sharing connectivity, the MnO_6 and NiO_6 octahedra undergo tilting in order to overcome the instability arising due to the ionic radii mismatch of the A and B'/B" site cations. This type of distortion is common in compounds that include very small A cations to occupy the 12-coordination site. This results in the 8 coordination A site in the monoclinic RNMO samples⁶⁹. The Ni/Mn-O bond lengths are limited to a narrow range. The Ni-O-Mn bond angles must distort with the octahedral tilts. In these tilted compounds the monoclinic β angle decreases as the r_R^{3+} value decreases.

In parallel the decrease of the ideal 180° Ni-O-Mn bond angle also takes place.⁷² This distortion leads to decrement of Ni-O-Mn bond angle from 180° .

In the notation developed by Glazer²⁰⁵ for representing tilt system $a^0a^0a^0$ is the aristotype cubic structure with $Fm\bar{3}m$ space group symmetry²⁰⁶. There are two types of tilt system possible in this crystal structure depending on the axes through which the tilting occurs. By looking the crystal structure through monoclinic $P2_1/n$ $[110, \underline{1}10]$ axes, successive octahedra undergo antiphase tilting down these axes. However, along the monoclinic $P2_1/n$ $[002]$ axis, successive octahedra undergo an in-phase tilting²⁰⁴. In this tilt system equal magnitude of subsequent octahedral tilts with opposite direction about the pseudo cubic a and b axes can be viewed. Hence the representation for this tilt system is $(a^-a^-c^+)$. While another tilt system in which in-phase tilting along $[01\underline{1}]$, and an antiphase tilting along $[011, 21\underline{1}]$ axes lead to $(a^+b^-b^-)$. Hence Glazer representation of the two octahedral tilting systems for the $P2_1/n$ monoclinic phase of PNMO is written as $(a^-a^-c^+)$ and $(a^+b^-b^-)$ ^{9,207}.

In PNMO films the ordered Mn/Ni site arrangement can be stabilized through moderately high temperatures and high oxygen pressure growth of the films. These films remain in short-range order regardless of growth conditions¹⁹⁹. There is a presence of small amounts of randomness in configuration of Mn and Ni even in completely ordered monoclinic structure. These disorders are of different kinds based on the way it is distributed within the lattice. First one is the antisite (AS) defect, where Ni and Mn cations just interchange their sites. Slight volume of such AS defects is predicted to occur due to configurational entropy. antiphase boundary (APB), is another type of disorder which parts two ordered domains with inverted Ni and Mn site occupancies. This can be explained in other ways as building up of AS disorders in one place, forming the exact pattern of the ordered phase, but in the opposite direction²⁰⁸. This results in Mn^{4+} - Mn^{4+} and Ni^{2+} - Ni^{2+} anti-ferromagnetic interactions. When the antisite defects and random occupancies are high, then Mn^{3+} and Ni^{3+} regime forms, in which superexchange mechanism is through antiferromagnetic interactions. Consequently, secondary magnetic transition or occasionally a glassy state at low temperatures can happen.^{97,121,122,174,197,199}. Furthermore, compared with the well-studied LNMO and NNMO compounds, the values of saturation moment in magnetization studies reveal that PNMO can be obtained with negligible anti-site defects²⁶.

XPS Analysis of PNMO

Pr 3d XPS spectrum and Mn and Ni 2p XPS spectrum in fig:2 Li *et al.*¹⁶⁸ reveals the presence of Pr³⁺ valence states and the mixed valency of Mn⁴⁺/Mn³⁺ and Ni²⁺/Ni³⁺ in PNMO^{168,198}. In the Pr 3d XPS spectrum, two broad peaks corresponding to Pr 3d_{3/2} at 954 eV and Pr 3d_{5/2} at 933 eV confirms the existence of Pr³⁺ in PNMO material. Shake off Satellites is observed in the lower binding energy regime for this doublet²⁰⁹. Peaks corresponding to Pr⁴⁺ are at 925.5 eV and 943.3 eV²⁰⁹. Since these peaks are absent in the XPS, spectra reveal that in PNMO Pr is at 3+ oxidation state. For Mn 2p spectra, the Mn 2p_{1/2} is assigned to peak at 652 eV and Mn 2p_{3/2} at 641 eV. For Ni 2p spectra the peak at 872 eV is of Ni 2p_{1/2} and at 854 eV is of Ni 2p_{3/2}. The presence of binding energy peaks of Mn³⁺, Mn⁴⁺ in Mn 2p spectra (Mn³⁺ 2p_{1/2} - 651.9 eV, Mn³⁺ 2p_{3/2} - 640.8 eV, Mn⁴⁺ 2p_{1/2} - 653.8 eV, Mn⁴⁺ 2p_{3/2} - 642.3 eV) and presence of Ni²⁺, Ni³⁺ in Ni 2p spectra (Ni²⁺ 2p_{1/2} - 871.64 eV, Ni²⁺ 2p_{3/2} - 853.96 eV, Ni³⁺ 2p_{1/2} - 873.62 eV, Ni³⁺ 2p_{3/2} - 855.55 eV) confirms that Ni and Mn in PNMO are in mixed valence state²¹⁰. Because of the presence of mixed states of Mn⁴⁺/Mn³⁺ and Ni²⁺/Ni³⁺, Bull *et al.*¹²⁰ reported small polar hopping conductivity of the sample at room temperature. Moreover, the percentage contribution of each valence state is calculated as 58.38%, 41.61%, 70.70%, 29.30% for Mn³⁺, Mn⁴⁺, Ni²⁺, Ni³⁺ respectively^{168,198}. The B site cation disorder has an effect on the oxidation state of Mn and Ni. In ordered samples oxidation state combinations of Ni²⁺/Mn⁴⁺ can occur, but more disordered samples exhibit Ni³⁺/Mn³⁺ states^{115,117,119}. For example, Asai *et al.*^{181,211} have done NMR spectroscopic analysis of LNMO in which the ordered compound had Mn⁴⁺ state, while Mn³⁺ state is shown by Mn ions in the Antisite defect.

Nazir *et al.*¹²¹ have done EXAFS analysis of RNMO (R=La to Ho) to estimate the local environmental changes in the (Mn/Ni) O₆ octahedra and Mn/Ni-O bond lengths. A main peak at ~ 1.35 Å appears in the EXAFS spectra. This matches the first coordination shell of Mn to the six oxygen atoms. A projecting peak around 1.44 Å indicates the Ni-O coordination cell.

Raman Analysis with PNMO

Raman spectroscopy is useful in examining the crystalline structure, spin-phonon coupling, disorder of cations, presence of impurity phases and local/dynamical lattice distortion in the double perovskite structure^{34,212}. No Raman active vibrational modes are observed for the ideal cubic perovskite structure¹²⁰. Rotation/tilting of octahedra, displacements of the A or B cations, or B site ordering leads to alterations from cubic symmetry. This results in the

symmetry reduction and Raman active modes will originate at the Brillouin zone centre. In Raman spectra the number of peaks and the relative intensity of these peaks is associated with extent of alteration from the aristotype cubic structure ¹²⁰. Raman spectroscopy is a non-destructive tool to differentiate between the monoclinic $P2_1/n$ and the orthorhombic $Pbnm$ perovskite structure; this is probable due to selection rules and the different symmetry of the corresponding Raman modes ^{213,214}.

Singh ¹⁹⁹ have analysed the micro-Raman spectra of PNMO films in XX, XY, X'X', X'Y' scattering configurations. In this X and Y represent the horizontal and vertical polarization directions, while X', Y' represent diagonal directions to X and Y. The significant intensity reduction in the XY mode and absence of these modes in the X'Y' configuration proposes the monoclinic and/or orthorhombic symmetry of PNMO material ^{215,216}. In some reports these Raman spectroscopic arrangements are represented as HH (XX) and HV(XY). corresponding to parallel and perpendicular directions of configurations of polarized Raman spectroscopy arrangement. Experimentally, for PNMO monoclinic ($P2_1/n$) phase two sharp peaks are detected in two polarization configurations (HH, HV) is shown in Truong *et al.* ⁸⁷ in figure 3 and Mayer *et al.* ²¹⁷ in figure 2.

Depending on the polarization arrangement there is variation in the relative intensity of Raman peaks. ¹⁹⁹ In the Raman spectrum of PNMO two strong modes around 650 cm^{-1} (A_g) and 500 cm^{-1} (B_g) were observed ^{87,120,121,199}. These vibrational modes are due to the symmetric stretching of (Ni/Mn)O₆ octahedra (breathing mode) ^{213,217,218} and mixed kind of antisymmetric stretching and bending motions (mixed mode) ^{121,217}.

The mode at 650 cm^{-1} is having A_g symmetry, which is acceptable in HH configuration. Relatively less intensity of this mode is found for crossed HV scattering arrangements. The phonon mode at 500 cm^{-1} exhibits B_g symmetry with high intensity at HV configuration and comparatively less intensity at HH configuration ^{213,218–220}. The crystallinity of the grown PNMO films can be indicated by the modes around $\sim 1200\text{--}1350\text{ cm}^{-1}$. These additional modes are the second order overtones of the A_g and A_g/B_g mode combination ²²⁰. Around the low frequency region ($\sim 300\text{ cm}^{-1}$) feeble stretching modes indicate $P2_1/n$ monoclinic symmetry. For the confirmation of the pure phase of the samples there is absence of Raman peak around 377 cm^{-1} corresponding to most of the rare earth oxides ²²¹.

The broadness in the Raman modes is due to the antisite disorders. The disordered Ni and Mn sites contribute different Ni-O and Mn-O stretching vibrations. These unresolved vibrations

having similar frequency in the B'/B" sites also added up in the band of Raman modes that increase the bandwidth ¹⁵¹. As sample cools, softening of A_g mode is observed, which is initiated at the transition temperature and continues as progressively cools the sample ²¹⁷. Truong *et al.* ⁸⁷ in figure:4 express the shift in the A_g mode and B_g mode in Raman spectrum with temperature. This softening may be due to two reasons, first one is that the interconnection between Ni/Mn–O exchange interaction and force constant may be negligible. Second reason is that the variation of the exchange interaction is feeble by itself due to temperature change in PNMO ⁸⁷. As progressively cool the samples an increase in intensity of the phonon excitations and a decrease in their linewidth is observed. This indicates the low temperature reduction of phonon scattering and improved Raman tensors due to reinforced orbital polarization.

The dependence of temperature on the frequency of the phonons have two main origins; (i) anharmonicity ²²², and (ii) spin–phonon coupling ²²³. For anharmonic term, the position of the phonon obeys Balkanski's model as the temperature changes ²²². That considers the anharmonicity contributions with the relation,

$$w(T) = w_0 - C \left[1 + \frac{2}{\left(e^{\frac{\hbar w}{kT}} - 1 \right)} \right]$$

with C and ω_0 being fitting parameters.

Spin phonon coupling is related to phonon renormalization as a consequence of magnetic ordering. This is because of the coupling between magnetic ordering and lattice ^{110,215,224}. The contribution of spin–phonon coupling $(\Delta w_{ph})_K$ to position change of the kth phonon is expressed as ²²³

$$(\Delta w_{ph})_K = \sum_{i,j>i} J_{ij} \langle s_i \cdot s_j \rangle$$

J_{ij} represent the super exchange integral and $\langle s_i \cdot s_j \rangle$ refers to the spin correlation function. Here to arrive at this relation it is considered that the magnetostriction effects and electronic states renormalization are absent and also considered only the first-neighbour interactions. Also, a molecular field approximation, can be considered in the case of the stretching phonon, as

$$(\Delta w_{ph})_K \propto \left(\frac{M(T)}{M_0} \right)^2$$

$M(T)$ is the magnetization at a particular temperature T , and M_0 is the maximum magnetization obtained.^{110,223}

When the rare earth ion of RNMO has changed with another rare earth ion, the shifting of Raman peaks is observed. The decrement of r_R^{3+} shows a shifting of A_g mode towards lower wavenumbers is observed. This is due to the decrease of force constant of the perovskite lattice with increase in the Ni/Mn -O bond length. This results in symmetric stretching mode to shift to higher wavenumber. Hence decrease in the A cation radii leads to the reduction in the superexchange interaction and also spin phonon coupling²¹⁷. The spin phonon coupling interrelates the magnetic and phonon properties. This kind of behaviour is also shown by rare earth manganites $RMnO_3$ ^{225,226}.

Truong *et al.*⁸⁷ reported the beginning of peak softening is around 100 K for polycrystalline PNMO samples, which is far below the T_C of PNMO at 228 K (Fig:10). Compared with the values for the softening of A_g mode in LNMO, which is around 7 cm^{-1} from T_C to low temperatures ($\sim 10\text{ K}$), the softening of PNMO is small $\sim 1.5\text{ cm}^{-1}$ ^{1213,216,218,227}. These results predict that the influence of force constant on the variation of Ni/Mn and O ions exchange interaction is small in PNMO²²⁶. Another study of PNMO thin films, around the ferromagnetic transition temperature 214 K the softening of peak (A_g) is observed¹⁹⁹. Temperature dependence of the A_g mode in epitaxial film and in polycrystalline bulk sample are pictured by Singh *et al.* in figure:4¹⁹⁹. This softening is only about 2 cm^{-1} , which indicates a weak spin phonon coupling.

Compared with the Ni, Mn system (PNMO) for the Co, Mn system (PCMO) The B–O stretching modes observed about $20\text{-}30\text{ cm}^{-1}$ higher wavenumber^{120,217}. Clarifications on this regard is that in the Ni-Mn system, the Ni/Mn–O and Pr–O bonds have a better extent of overlapping compared with the Co-Mn scheme. The large extent of orbital overlapping observed in the Ni-Mn system reduces the bond length. Also, the bond strength can be changed by varying transition metal charge density^{120,217}. Meyer *et al.*²¹⁷ reported A_g mode softening in PNMO is initiated at T_C around 220K and further increased by successive cooling²¹⁷. The weak impact of Co^{2+} and Ni^{2+} cations on the spin-phonon coupling is indicated by slight change in the spin-phonon coupling strength, for the same A-site cation. In general, the R_2CoMnO_6 (RCMO) film series shows slightly larger values of spin phonon coupling strength (only

exception R = La) than the RNMO film series²¹⁷. As the cation size of Co²⁺ and Ni²⁺ is similar¹⁸⁰ and the lattice parameters are also comparable, apart from the extent of overlapping, other factors like the different spin contributions of HS-Co²⁺/Ni²⁺, and their impact on the bonds, force constants, and phonon properties may involve in this regard. The impact of B site ordering and the spin phonon coupling in double perovskite is investigated in the study of Gd (Co, Mn) O₃ and its spin phonon coupling observations²²⁴.

Magnetic properties

Magnetic properties of PNMO are related to the Ni-O-Mn bond angle and the covalency/ionicity of Ni/Mn-O bond. Thermo magnetization curves FC and ZFC are used to study the magnetic properties of these systems. In Field cooled cooling (FCC) approach the sample is cooled from a higher temperature along with an application of magnetic field and throughout the procedure recording the magnetization. The temperature was then increased with applied field and measured the magnetisation (FCW). However, in the ZFC protocol the sample cooled in the absence of a magnetic field. Then the magnetization is measured by increasing the temperature along with the magnetic field. Magnetization plots in zero field cooled (ZFC) and field-cooled (FC) protocols show a divergence between FC and ZFC at low temperature. Lekshmi *et al.*¹⁶⁷ in figure :2 show the thermo magnetization field-cooled (FC) and zero-field-cooled (ZFC) curve of PNMO and dM/dT versus T. The applied magnetic field is 500 Oe. The divergence initiated near the transition temperature. This indicates competing magnetic interactions like spin glass or cluster glass^{31,121,167}. Due to magneto crystalline anisotropy resulting from the spin-orbit coupling between the Ni-Mn network and Pr ions^{88,122,166}. Variation of dm/dT with T and it shows only one magnetic transition for PNMO. The lower magnetic transitions occurred due to the presence of antiphase boundaries that are absent in the material. This confirms the ordered arrangement of PNMO compared to many other RNMO samples.

Near room temperature, the PNMO sample is paramagnetic. While, with decreasing temperature a magnetic transition is observed around 200 K. The critical temperature varies from 208K to 255K in different reports^{26,88,121,122,166,198-200}. Paramagnetic curie temperature obtained from Curie Weiss plot has values 218 to 226 K^{88,121,122}. Observed effective paramagnetic moment (Results from fitting to the Curie-Weiss plot by the equation $\mu_{eff} = 2.828 \sqrt{C}$)¹⁹⁵ ranges from 6.124 to 8.41 $\mu_B/f. u.$ ^{121,122,200}. Effective magnetic moments can obtain using the equation^{121,155} :

$$\mu_{eff}(calc) = [2\mu_B(Pr^{3+})^2 + \mu_B(Ni^{2+})^2 + \mu_B(Mn^{4+})^2]^{1/2}$$

Reported μ_{eff} (Calc) values are 6.32 to 7.14 $\mu_{\text{B}}/\text{f. u}$ ^{121,122,200}. Measured saturation moment (M) has values from 4.92 to 5 $\mu_{\text{B}}/\text{f. u}$ ^{26,121,122,199,200}. From the M vs 1/H plot The extrapolation to 1/H =0 will give the value of saturation moment ($M_{\text{extrapolated}}$)^{121,122} reported as 5.48 to 6.69 $\mu_{\text{B}}/\text{f. u}$ ^{121,122,200}. Theoretical saturation moment $M_s = [2g_J + 5.0] \mu_{\text{B}}/\text{f. u}$ ¹²¹, where g_J is the rare-earth saturated moment, and 5 $\mu_{\text{B}}/\text{f. u}$ is the effective magnetic moment of the Ni-Mn system. M_s is in the range 11.4 to 13.7 $\mu_{\text{B}}/\text{f. u}$ ^{121,122,200}

Effective magnetic moment μ_{eff} calculated for possible spin state configurations of Ni and Mn in PNMO	
Spin systems	$\mu_{\text{eff}}(\text{calc}) = [2(\mu_{\text{Pr}})^2 + (\mu_{\text{Ni}})^2 + (\mu_{\text{Mn}})^2]^{1/2}$
Mn ⁴⁺ (S = 3/2), Ni ²⁺ (S = 1)	6.971
Mn ³⁺ (S = 2), Ni ³⁺ (S = 3/2)	8.035
Mn ³⁺ (S = 2), Ni ³⁺ (S = 1/2)	7.252
Mn ²⁺ (S = 2), Ni ⁴⁺ (S = 2)	8.578
Mn ²⁺ (S = 2), Ni ⁴⁺ (S = 1)	7.589
Mn ²⁺ (S = 2), Ni ⁴⁺ (S = 0)	7.042

$\mu_{\text{Ni}} / \mu_{\text{Mn}}$ (spin only systems) = $[g S(S+1)]^{1/2}$; $g = 2$ for Mn and Ni
 $\mu_{\text{Pr}} = [g_{\text{Pr}}^2 J(J+1)]^{1/2} = 3.578$
 $g_{\text{Pr}} = \frac{3}{2} + \frac{S(S+1) - L(L+1)}{2J(J+1)} = 0.8$ (S = 1, L = 5, J = 4)

In the table 4 the effective magnetic moment of all the possible oxidation states of Ni and Mn are calculated for comparison.^{228,229} From the values the experimentally determined values are in correlation with the oxidation state of ordered Mn⁴⁺ and Ni²⁺ and Mn³⁺ and low spin Ni³⁺. The Ni⁴⁺ (s=0) and Mn²⁺ (s=2) also have values of magnetic moment in the range of experimentally obtained results. But the zero spin of Ni⁴⁺ can enable the choice of this pair of ions in the PNMO material. The studies with NMR and XAS¹¹⁵⁻¹¹⁷ show the actual valence states are Ni²⁺ and Mn⁴⁺. The theoretical and experimental correlation of these values is due to the consideration of spin only systems Mn⁴⁺ and Ni²⁺ with $\mu_{\text{eff}}(\text{Mn}^{4+}/\text{Ni}^{2+}) = g\sqrt{s(s+1)}\mu_{\text{B}}$ and Pr³⁺ with $\mu_{\text{eff}}(\text{Pr}^{3+}) = g\sqrt{J(J+1)}\mu_{\text{B}}$ since J is considered a good quantum number for lanthanides. The difference in the effective paramagnetic moment value for experiment and theoretical is associated with the crystal field splitting. In the presence of oxygen ligands on the MnO₆ and NiO₆ octahedra the degenerated d orbitals will split into t_{2g} and e_g states. The e_g state is having the higher energy in the spherically symmetric environment.¹⁸⁶ The filling of electrons in these orbitals is based on Hund's rule as a consequence of the competition between the coulomb

energy and crystal field energy. In certain systems the crystal field splitting is stronger than the spin orbit interaction. This is called orbital quenching.²³⁰ For 4f electrons, the orbitals are near to the nucleus and inside 6s and 5p. Hence the crystal field is shielded by the 6s and 5p electrons. For 3d electrons the shielding of 4s electrons is not as strong as that for 4f electrons. This confirms the prominent crystal field splitting of these compounds which leads to the orbital quenching and becomes spin only systems. The critical temperature of PNMO is less than LNMO and greater than other members of RNMO series which have ionic radius less than Pr. Which can be explained on the basis of the change in superexchange angle discussed before.

Antiphase boundaries formed due to the antisite defects at Ni/Mn site leads to a negative ZFCM(T) in PNMO in the study done by Nazir *et al.*¹²¹ ferromagnetic coupling of short-ranged order forms among Ni²⁺ and Mn⁴⁺ cations. While in the antiphase boundaries coupling is antiferromagnetic in nature. It is impossible to align these opposite spins in line with the direction of magnetic field at relatively lower magnetic field strength in the ZFC mode in anti-phase boundary. As temperature is increased the antiparallel or tilted spins get weakened¹²¹. The thermo magnetization curve obtained from the field cooled protocol shows a rapid increase in magnetization T_c which is due to the ferromagnetic ordering of Ni²⁺ and Mn⁴⁺ sub lattice. For higher temperature this upturn moves to higher temperature, which is the common feature of ferromagnetic interaction¹⁸⁸.

Troung *et al.*⁸⁷ and Harisankar *et al.*³¹ reported a secondary magnetic transition around 126K for PNMO thin films, which arises due to the presence of anti-phase boundaries. Ali *et al.*¹⁸⁸ theoretically reported for PNMO samples around 27 K there is a downturn in magnetisation at 27K in low magnetic fields. This downturn in the magnetic field can suppress and change to an upturn at larger magnetic fields^{187,188}. There is a slight disagreement with the experimentally obtained results for PNMO. There is no downturn in M_Z at low temperature in the low field data of PNMO. Magnetization (M_Z) as a function of temperature (T) at various strength of external fields the for the experimental and theoretical (Monte carlo results) are explained with figure:1 and figure:5 by Ali *et al.*¹⁸⁸ This may be due to smaller spin orbit coupling in PNMO that can be easily overcome even by a small magnetic field. The experimental findings are supported via Monte Carlo simulations and mean field analysis on the two-sublattice Heisenberg model¹⁸⁸ for other rare earth ions R=Nd, Sm, Dy Gd, Tb. Rare earth ions magnetic moments appear only at low temperature characteristically below 30 K¹⁷⁹. In some reports this secondary magnetic transition below 30 K is seem to be the result of antiferromagnetic coupling between R ion (Pr, Nd, Sm) and Ni-Mn sublattice and ferromagnetic for R = Gd, Tb,

Dy^{182,191,231}. However recent DFT analysis on Nd₂NiMnO₆ reveals that magnetic spin between Nd spin and Ni-Mn sublattice is ferromagnetic in nature. Hence Ali *et al.*¹⁸⁸ Explain this secondary transition as, for less than half filled 4f shells the orbital moment of the R ion is oppositely aligned to spin moment and is larger in magnitude than spin moment. Even though the spin is coupled ferromagnetically to the Ni-Mn sublattice the orbital moment is opposite to the spin moment, resulting in a downturn in magnetization. At large enough magnetic fields, it becomes energetically favourable for the net effective magnetic moment to align with the field, which leads to a switching of the magnetization anomaly at 27K from a downturn to an upturn as the field is increased.

Nevertheless, many of the reports^{26,121,122,167,199,200} establish single magnetic transition in PNMO which arises due to the Ni²⁺-O-Mn⁴⁺ superexchange interaction and also absence of the secondary transitions is an implication of less disordered samples.

In the 1/χ vs. T the high temperature region data are fitted perfectly with a Curie – Weiss (CW) law with positive θ values. This is an indication of the supremacy of the ferromagnetic relationship of spins in this system^{121,122,166,167,200}. Reports on saturation magnetization reveal the ideal value 5μ_B for complete ordered samples^{122,200}. The slightly lower values than the 5μ_B indicate the presence of a small amount of antisite disorders^{26,166,199}. All paramagnetic temperatures obtained from the Curie- Weiss plot is positive. That proposes the predominant exchange interactions as ferromagnetic.

Observation of a significant Magnetic caloric effect (MCE) in double perovskite RNMO opens up possibilities for using the high degree of flexibility available in these oxides to enhance the effect further. Properties such as Superexchange interaction, low value of coercive field and high saturation magnetic moment for rare earths with high magnetic moment are vital for magnetocaloric refrigerant.

Based on thermodynamic theory, for a range of magnetic field ΔH the change in temperature and the corresponding magnetic entropy change (−ΔS_M) is expressed as,

$$\Delta S_M(H, T) = \int_0^H \left(\frac{dM}{dT} \right) \left(\frac{dM}{dH} \right)_{H'} dH'$$

Relative cooling power (RCP) is used to quantify the usefulness of MCE materials which is defined as^{88,188}

$$\text{RCP} = -\Delta S_M(T, H) \times \delta T_{FWHM}$$

Ali *et al.*¹⁸⁸ recently published a paper in which comprehensive experimental and theoretical study of magnetization and magnetic caloric effect of RNMO materials was reported. Distinct behaviour depending on the choice of R is observed at low temperature. This low temperature anomalies in magnetization manifest in the change in the entropy $-\Delta S$ whose sign depends on choice of R. Magnetic entropy changes versus temperature at different applied magnetic fields up to 8T for PNMO shows two prominent features (Fig:13). First one is at the ferromagnetic transition temperature T_C and second one at lower temperature (T_2)¹⁸⁸. The value of $-\Delta S_M$ is positive across T_C and its magnitude increases with field, which is consistent with the ferromagnetic ordering of the Ni-Mn sublattice at T_C . When the temperature is lowered $-\Delta S_M$ monotonically decreases below T_C . On increasing the magnetic field this decrease can be suppressed and a positive peak or anomaly appears at low temperature and high fields. This can be realised as the opposite alignment of the total effective moment of the R ions with the Ni-Mn sublattice below T_C at low fields. So, the magnetic entropy is high. At higher fields, the R moment switches and aligns with the Ni-Mn sublattice and also the applied magnetic field, resulting in a low magnetic entropy like in the case of the ferromagnetic transition at T_C . Using mean field approximation and Monte Carlo simulations on the minimal spin model the key features of the experimental results are verified. The anti-alignment of Pr with Ni-Mn sublattice at low temperature leads to $-\Delta S_M < 0$ (not observed experimentally). This comparison of experimental and theoretical results is shown in figure:3 and figure:7 by Ali *et al.*¹⁸⁸ At sufficiently high magnetic fields this external field can enforce the alignment and hence the inverse magnetocaloric effect can change to magneto caloric effect. The change in entropy with the Temperature graph also does not match with the experimental results.

Electrical properties

The electronic band gap of RNMO samples depends on the orbital overlap of the different elements involved in the crystal structure. The bond angle and bond length can be used to estimate the bandwidth^{232,233}. The electrical resistivity and the band gap in these perovskites²³⁴ mainly administered by the B–O sublattice. orbital overlaps along the distorted cube edges lead to the formation of bands. the geometrical factors; super exchange angle, and the characteristics of TM ions at B'/B'' sites determine the magnitude of the orbital overlap. As superexchange angle decreases orbital overlapping reduces, consequently the hopping of

electrons between TM ions via superexchange interaction decreases⁹⁵. The decrease in the orbital overlap makes the conduction band and valence band more separated in energy. Hence there is a possibility of band gap increase with r_R^{3+} decrement, and an increased tilting angle of octahedral^{120,121,176}. However, there are contradictory reports which claim the RNMO based double perovskites band gap remains largely unaffected due the charge transference from oxygen to Mn^{4+} and Ni^{2+} ²⁶. According to this concept, electron hopping integrals and orbital band width is not influenced by the Mn-O-Ni bond angles and the Mn/Ni-O bond lengths in the material. However, variation in super-exchange strength changes T_C ²⁶. This is manifested from high pressure analysis on LNMO that holds the ferromagnetic character, with a minor disparity in T_C and magnetic moment decrement even under 30 GPa pressure²³⁵. Polycrystalline materials show orders of magnitude difference in resistivity due to the grain boundaries. That is some of the insulating compounds are in fact poor metals and which show poor resistivity due to grain boundaries²³⁶⁻²³⁸. An example for that is La_2NiCoO_6 ²³⁹. Balasubramanyam *et.al.*²⁶ from the $O1s$ XAS edge spectrum of PNMO obtained in the total electron yield mode, determines the band gap energy. For determination of E_F , spectrum of $LaNiO_3$, which is a metallic compound, and $LaMnO_3$, with a known band gap is used. At the rising edge of $LaNiO_3$ the position of E_F was fixed. Around 1.1 eV above E_F there is a rise in spectra for $LaMnO_3$. This can be considered as the band gap of $LaMnO_3$. From optical conductivity measurements the bandgap of 1.2 eV has been obtained²⁴⁰. In the same method the bandgap of PNMO is calculated as 0.9 eV. This method of band gap determination from $O1s$ spectrum is not reliable because of the effects of $O1s$ core hole²⁶. However, an understanding of the range of the band gap values can be obtained. The value obtained from resistivity measurements is around 0.65 eV and a greater bandgap value is obtained as 0.75 eV through charge transfer studies. The density of states analysis shows a band gap of 1.2 eV for $U-J > 2$ eV then further constant for $U-J = 8$ eV²⁶. Density of states analysis reveals the P-d type band gap of PNMO material. From four probe measurements the band gap is obtained as 1 eV¹²⁰. From UV Visible absorption spectroscopy using τ auc plot the band gap energy is reported as 1.42 -1.5 eV¹²¹. Antisite disorders that are insulating regions are having an impact on experimental band gaps. The voids created while pressing the powders and the intrinsic effects of grain boundary leads to the changes in the exact result of resistivity. Also due to the addition of carrier production effects which are temperature dependent results in the alteration of resistivity and band gap values⁶⁰.

Dielectric properties

The two parameters of dielectric material, the relative dielectric constant and $\tan\delta$ of PNMO with various temperatures, are shown in figure :3 Lekshmi *et al.*¹⁶⁷ The complex dielectric constant of a material in the AC electric field can be characterized by: [16]

$$\varepsilon^* = \varepsilon' + i\varepsilon''$$

where ε' is the real part representing the energy storage (dielectric constant) and ε'' the imaginary part of complex permittivity, the loss of energy ($\tan\delta$) during each cycle of electric field.

Study on dielectric properties on RNMO samples done by Booth *et al.*¹²² reveals low dielectric constants ($\varepsilon = 15-25$) with no dispersion suggest that there is perhaps no microwave magnetocapacitance effect in these materials. Particularly in PNMO having ε is 23 and $\tan\delta$ is 0.013¹²². Small value of dielectric constants and loss tangent and high value of resistivity (10^7 V-cm at 300 K) of RNMO oxides are consistent with the ordered double perovskite structure²⁴¹. Lekshmi *et al.*¹⁶⁷ conducted the magneto dielectric study on PNMO material in which the frequency dependent ε' (T) and $\tan \delta$ (T) plot, a relaxor-like dielectric behavior is observed (Fig:14). T_{\max} is the temperature at which $\tan \delta$ reaches its maximum. As the measuring frequency increases the value of T_{\max} shifts to higher temperature. Double relaxations are observed in ε' (T) plots¹⁶⁷. By using Koops-like model the experimental results can be explained which assumes this material as a multilayer capacitor²⁴². Hopping mechanism of electron among Ni /Mn ions is the reason behind the dielectric relaxation arising from the grains? From the results, the effect of a 'colossal dielectric constant' is obtained. This is due to the fact that in addition to the relaxation due to electron hopping, at higher temperature the grain boundaries reach 'conduction relaxation' state as well. At a higher temperature the increase of ε' will occur because of the fact that the necessary condition for a rapid relaxation time for higher frequencies. Increases in T_{\max} and E_{a1} with decrement in the radius of rare-earth ion ($r_{R^{3+}}$) obviously point out the electron hopping mechanism that is further suppressed with decrement in $r_{R^{3+}}$ ^{122,182}. The regular decrease of T_{\max} and E_{a1} with the $r_{R^{3+}}$ indicates that the magnetic and dielectric properties are related with the crystal structure of PNMO. The Ni-O-Mn bond angle decreases with decrease in $r_{R^{3+}}$. This in turn results in the decrease of overlapping of the orbital. That reduces the hopping of electrons between Ni and Mn. Hence results in the decrease in T_c and increase in T_{\max} and E_{a1} for dielectric relaxation. It shows interconnection between the magnetic properties with dielectric properties of RNMO. This

correlation is an indication of a spin phonon coupling which is really important for spintronics applications¹⁶⁷.

A site modification in PNMO

Rare earth ions have a great role in modifying the superexchange interaction and consequently the magnetic and electrical properties. Modification of the A site having Pr^{3+} ion with other elements will lead to the alteration of various properties of PNMO material. One of the studies for Ca doping in PNMO is used for the electrochemical applications. XPS analysis of the Ca doped PNMO which forms $\text{Pr}_{2-x}\text{Ca}_x\text{NiMnO}_{6-\delta}$ ($x = 0.0 \sim 0.3$) (PCNMO_x) were studied¹⁹⁸. The presence of Ca^{2+} valence state was obtained. The occupancy of the Ca^{2+} in Pr^{3+} site will increase the defect states which lead to the increase in electrical conductivity of these samples. Glycine nitrate method is used to prepare PCNMO_x double perovskite with monoclinic ($\text{P2}_1/\text{n}$) crystal structure. As the Ca^{2+} doping increases the oxygen vacancies in the lattice also increases. This in turn results in the increment in the unit cell volume and thermal expansion coefficient. δ value of oxygen vacancies in PNMO_x for $x=0$ is determined from the XPS spectra as 0.08. This gradually increases to 0.22 for $x=0.3$ ¹⁹⁸. Another modification is with La^{3+} ions to form LaPrNiMnO_6 . It has the same monoclinic structure. Since La^{3+} is having larger ionic radii than Pr^{3+} results in the increase in curie temperature compared to PNMO. It shows a magneto dielectric coupling in these samples.¹⁶⁶ Tang *et al.*⁴ investigated the photocatalytic application of LaPrNiMnO_6 . UV Visible analysis of Mesoporous LaPrNiMnO_6 shows the light absorption in the entire range of 200-700 nm indicates the effective absorption in the whole range and can be a good photocatalyst. This mesoporous structure has high oxygen content and better redox capacity. The activity of the catalytic oxidation of these samples also shows good results for the degradation of volatile organic pollutants.

Theoretical studies on PNMO

Zhao *et al.*¹⁷⁶ using first principal calculation studied the effects of chemical and hydrostatic pressures on structural, magnetic, and electronic properties of RNMO (R= Ce to Er) double perovskites. The structure correlation of many properties is explained on a theoretical basis. For both Ni^{2+} and Mn^{4+} the study has taken the Hubbard U value as 3 eV, which gives good correlation with the experimental results. For all the RNMO samples (R= Ce to Er) the value of mean Ni - O is larger than mean Mn-O bond length. The Ni-O bond lengths within these RNMO samples differ by less than 2.2% and the Mn-O bond lengths differ by less than 1.1% in comparison with experiments¹²². In the study they have tried to investigate whether applying

hydrostatic pressure on SNMO has the same effect as the chemical pressure in RNMO samples on the structural and magnetic properties. The effect of chemical pressure (change in $r_{R^{3+}}$) we have discussed in the comparison section of RNMO samples in this paper. While considering the hydrostatic pressure the lattice parameters, mean Ni- O and Mn-O bond lengths obtained as decreasing with increasing hydrostatic pressure. The monoclinic angle, antipolar displacement and the octahedral tilting angle has little effect on the hydrostatic pressure. The electronic band gap and the magnetic curie temperature slightly decreases as the hydrostatic pressure increases. The study proposes new predictions in anticipation of experimental validation. In contrast to the general concept for rare-earth perovskites, response of many physical quantities is in dissimilar manner to chemical and hydrostatic pressures which needs to be verified experimentally. Also, the effect of these pressures on antipolar displacements need experimental confirmation. Which need additional explanation for the effects of rare earth ion in inducing and tuning of electrical polarization of LNMO/RNMO superlattices¹³³. The effect of chemical and hydrostatic pressure on RNMO sample in Lattice parameters, Monoclinic angle, Bond length, tilting angle, Ni-O-Mn angle and Antipolar displacement are shown in figure:1 and figure:3 in the theoretical paper of Zhao *et al.*¹⁷⁶

2p XAS spectra indicate the presence of Mn^{4+} and Ni^{2+} states for PNMO. Charge transfer energies for Ni and Mn ions are calculated from the XPS spectra of each ion. PNMO obtained a higher electron count in comparison with the ionic values for the ground states of Ni^{2+} and Mn^{4+} ions. According to the Zannen-Sawatzky-Allen phase diagram²⁴³. PNMO is a charge transfer insulator with p-d type band gap and an intermediate covalent character²⁶. Ali *et al.*¹⁸⁸ reported recently that the choice of R, in addition to affecting the value of T_C , also influences the magnetization and consequently the MCE behavior as inferred from the nature of low-temperature anomalies for different R. In the paper they propose a simple explanation for this behavior in terms of a Heisenberg model that takes into account the coupling of the spin of rare earth ion with the spin of Ni-Mn network, as well as the local spin-orbit coupling on R site. The magnetic behavior at low temperatures in the double perovskites containing f block elements is controlled by spin-orbit coupling. More than or less than half filled 4f orbitals decide the nature of spin-orbit coupling to be ferromagnetic or antiferro-magnetic. The weak ferromagnetic coupling J between the rare earth ion sublattice and Ni-Mn sublattice and antiferromagnetic spin-orbit coupling (λ) in PNMO is responsible for the downturn in magnetization at low temperature. These calculations are confirmed with the Monte Carlo simulations¹⁸⁸. Pr_2NiMnO_6/La_2NiMnO_6 superlattice ground state structural electric and magnetic properties are investigated using first principal calculations²⁴⁴. The superlattice is

having a ferromagnetic ordering. Consistent with the antipolar displacement of Pr and La ions a ferroelectric polarization is predicted.

In the field of magnetic materials, the study of phase transitions is important. The magnetic transitions can be classified into two as first order and the second order^{245,246}. The detailed study of critical behaviour near the magnetic phase transition provides the knowledge about the microscopic interactions in the second order materials²⁴⁷⁻²⁵⁴. These critical properties can be analysed with four major theoretical models in second order transitions²⁵⁵⁻²⁵⁷. The magnetic transitions in most of the RNMO and RCMO compounds around paramagnetic-ferromagnetic (PM-FM) transitions are determined to be of second order transitions^{152,258-262}. Su *et al.* have studied the magnetic critical properties of the second-order PM-FM transition of RNMO (RE = Eu and Dy). The study reveals the critical behaviour of $\text{Eu}_2\text{NiMnO}_6$ are in between the mean-field and (3D) Heisenberg interaction models. For $\text{Dy}_2\text{NiMnO}_6$ the critical behaviour cannot be explained by any known theoretical model. This may be due to the nonexistence of long-range order in DNMO¹⁴⁰. The critical parameters for RNMO (R = Y, La) are very close to the 3D-Heisenberg theoretical model with a short-range FM order^{263,264}.

Applications

Electro chemical property and energy storage application

PNMO has been proved as a good candidate as cathode for Intermediate temperature Solid oxide Fuel cells (IT-SOFC). It exhibits high chemical stability, thermal expansion characteristics, with GDC (Gd doped $\text{CeO}_2 - \text{Ce}_{0.9}\text{Gd}_{0.1}\text{O}_{1.95}$) as electrolyte. Also shows promising electrochemical performance around 700°C in air. The electrical conductivity of PNMO is obtained as very low as approximately 3 S cm^{-1} at 800°C . By the optimization of the electrode microstructure and formation of composite electrodes the cathode efficiency can enhance.¹⁶⁸ Sun *et al.*¹⁹⁸ in figure :7 described the schematic of the ORR reaction mechanism and the impedance analysis plot for the PNMO cathode.

. Ca doping in PNMO and consequent electrochemical performance of $\text{Pr}_{2-x}\text{Ca}_x\text{NiMnO}_{6-\delta}$ were studied using AC impedance spectroscopic analysis at 700°C in air. The reaction mechanism of the cathode is not changed with calcium doping. The increment in the oxygen vacancies due to doping of Ca and corresponding enhancement in the conductivity results in the better electrochemical performance. The possible application of Ca doped PNMO for SOFCs has been verified with I-V and I-P curves of single cell. The long-term stability of this particular cathode material is obtained from the constant value of the voltage and power density

throughout the measurement ¹⁹⁸. Recently supercapacitor application of GNMO has been reported ¹⁴². This can be extended to PNMO material as well.

Photocatalysis

The higher oxygen content and redox capacity of the mesoporous double-perovskite catalysts LaPrNiMnO₆ can be used in the application of photothermal synergistic degradation of gaseous toluene. Schematic of the photocatalysis process involved in the material is shown in fig:18. Larger specific surface area and consequent increase in the reactivity of the catalyst are the important features of mesoporous structure. LaPrNiMnO₆ possessed high capacity for the adsorption of oxygen content and also absorption of light is obtained from UV vis and XPS spectra analysis. Which results in the occurrence of catalytic oxidation in Mars–van Krevelen redox cycle mechanism ²⁶⁵. LaPrNiMnO₆ exhibited better catalytic activity due to the lower activation energy in the reaction kinetics study of this material. This property opens the door into the wide application of RNMO and modified RNMO samples in the field of volatile organic pollutant degradation ⁴. Possible C₇H₈ degradation mechanism of LaPrMnNiO₆ under photothermal conditions schematically shown in figure :9 by Tang *et al.* ⁴

Magneto refrigerant material

This field of research is growing fast due to the characteristics of high conversion efficiency and ecological nature of magnetic cooling technology ^{247,266}. A magneto caloric study ¹⁵² in PNMO reveals relative cooling power of 41.35 JKg⁻¹ at 20 KOe and ΔS_{\max} at 215K (T_C = 213K) are 2.4 JKg⁻¹K⁻¹ and 4.9 JKg⁻¹K⁻¹ for 20 KOe and 50 KOe respectively. Zhang *et al.* ⁸⁸ reported the reversible magnetic caloric effect around T_C of ~208 K is correlated to second order magnetic transition. ΔS_{\max} value of 1.25 J/kg⁻¹K⁻¹ and RCP of 48.2 J/kg for ΔH in the range 0–2T and ΔS_{\max} value 2.48 J/kg⁻¹K⁻¹ and RCP of 150.1 J/kg for ΔH of 0–5 T. A study of PNMO and PCMO by changing the ratio of Co/Ni enabled the design of magnetocaloric composite material for use as magnetocaloric refrigerant in a wide temperature range ⁸⁸.

Spintronics

Spintronics is thought to have huge potential for the next generation of information technology, since information can be transmitted at higher speeds and with low energy consumption ²⁶⁷. Magnetodielectric property and the spin phonon coupling is pointing out that PNMO can be utilized for the spintronics applications ¹⁶⁷. Even though studies reveal that the

spin phonon coupling is weak in PNMO, further advance research in the application domain is not extensive. The important behaviour that PNMO is having for exhibiting the magneto dielectric property is ferromagnetic insulator with positive superexchange interaction. The bulk properties exhibited to be reproduced in thin films in order to make the PNMO based spintronics device become a reality. For the application in magneto electronics as non-volatile memories studies on perovskites has been done in order to explore the coupled electric and magnetic properties. This magneto dielectric or magneto capacitance are used in spintronics applications. For novel devices like multiple-state memory elements, electric-field controlled magnetic sensors etc the simultaneous existence of ferromagnetism and ferroelectricity with spin phonon and spin polar coupling is necessary.

In the domain of gas sensing, biological application and the research on LNMO and some of the members of RNMO have been carried out and show attractive results as well. This gives an insight to explore other members of the RNMO family to these applications. For the adsorption of bovine serum albumin (BSA) application study has revealed that LNMO shows a good absorbing ability to BSA²⁶⁸. These are a potential carrier for large biomolecules, which will be widely used in the biomedical field and in biotechnology. Gas sensing applications in LNMO have been done with the help of impedance measurement under various gaseous environments with varied concentration. Magneto impedance at the IT magnetic field shows a positive value for oxygen, negative value for argon and nearly zero for nitrogen atmosphere²⁶⁹. The various industrial applications are possible with this compound including non-volatile memories, capacitors, sensors, actuators, resonant wave devices (such as radio- frequency filters), infra-red detectors, optical switches, and electric-motor overload protection circuits with multiple function.²⁷⁰.

Conclusion and future prospect

In this review paper various studies on PNMO that have been done in different parts of the world are reported. While there are lots of questions that still need to be answered. Novel predictions obtained from the theoretical calculations that call for experimental confirmation regarding rare earth double perovskites are

- (i) The differences in response in terms of qualitative and quantitative aspects of various physical properties to hydrostatic pressure and chemical pressure.
- (ii) How hydrostatic and chemical pressure depends on the antipolar displacements.

So, validation of these predictions through experimental analysis is needed. From Analysing the various studies on RNMO and specifically PNMO the rare earth ionic radius influences the Mn-O-Ni bond angle which correlates with the superexchange interaction. Hence Doping the A' site and/or B' site of PNMO can lead to changes in the magnetic, electric and spin phonon coupling properties. When an additional magnetic ion is doped either in A site and/or B'/B" site of the PNMO the changes in the magnetic behaviour and the variations in the conduction mechanism as well as the dielectric study after the doping are yet to be done with this material. The Neutron diffraction and soft x-ray scattering is warranted to study the temperature dependence of the structural properties and the ion positions, to explore the origin of the spin-phonon coupling obtained from the Raman study of PNMO. Neutron diffraction studies are necessary for the confirmation of the ordering of double perovskites, which strongly influence magnetic and electric properties. Studies on PNMO based on neutron diffraction are very few. If studies are extended in that direction as well, there will be many possibilities to unveil the vast and unique properties of the PNMO double perovskite. The low temperature spin glass behaviour of PNMO samples is not studied much in detail. The studies are done only as a comparison with other RNMO samples in this field of magnetism. Hence the glassy nature and the canted spins of the lattice and the coupling of Ni Mn an Pr magnetic ions leads to much complex magnetic behaviour. The study on these magnetic interactions provides insight to the richer phase diagram of these PNMO materials for both experimental and theoretical domain. The variable valence state of Ni and Mn leads to additional exchange interactions which will affect the phase transitions. So, the much-detailed study of PNMO with the help of XPS, EXAFS together with the magnetic study provide details about the local atomic structure and the influence of the valence state with the magnetic interactions in this particular member of RNMO family. Electrical properties with the determination of band gap and the conduction mechanisms need further studies in PNMO since these studies particularly on PNMO is very less. A site ordering of this family of double perovskites also needs attention for comparing the modulation of properties in these different arrangements. The thorough understanding of the spin as well as oxidation states of Ni and Mn cations is necessary to study the magnetic response of these systems. X-ray-absorption spectroscopy (XAS), which probes into the local atomic structure can be used to explore the short-range order and the exciting characteristics behind the PNMO double perovskite. These techniques which give details about the local structure of PNMO samples can also be utilized for further understanding of the exciting world of this particular double perovskite material. Hence detailed study of the structure correlation

of PNMO and other members of the RNMO family is important in terms of probing the useful properties which call for practical applications.

REFERENCES

- ¹ F. Gheorghiu, L.-P. Curecheriu, I. Lisiecki, P. Beaunier, S. Feraru, M.N. Palamaru, V. Musteata, N. Lupu, and L. Mitoseriu, *Journal of Alloys and Compounds* **649**, 151 (2015).
- ² S.-W. Cheong and M. Mostovoy, *Nature Materials* **6**, 13 (2007).
- ³ F.J. Garcia-Garcia, M.J. Sayagués, and F.J. Gotor, *Nanomaterials* **11**, 380 (2021).
- ⁴ Y. Tang, Y. Tao, Q. Wang, Z. Zhu, W. Zhang, X. Li, A. Xie, and S. Luo, *Journal of Materials Research* **34**, 3439 (2019).
- ⁵ M. Moullem-Bahout, T. Roisnel, F. Bourée, G. André, C. Moure, and O. Peña, *Progress in Solid State Chemistry* **35**, 257 (2007).
- ⁶ T. Ferreira, G. Morrison, J. Yeon, and H.-C. zur Loye, (2016).
- ⁷ S. Vasala and M. Karppinen, *PROGRESS IN SOLID STATE CHEMISTRY* **43**, 1 (2015).
- ⁸ F. Li, M.J. Cabral, B. Xu, Z. Cheng, E.C. Dickey, J.M. LeBeau, J. Wang, J. Luo, S. Taylor, and W. Hackenberger, *Science* **364**, 264 (2019).
- ⁹ P.M. Woodward, *Acta Cryst B* **53**, 32 (1997).
- ¹⁰ N.S. Rogado, J. Li, A.W. Sleight, and M.A. Subramanian, *Advanced Materials* **17**, 2225 (2005).
- ¹¹ G. King and P.M. Woodward, *Journal of Materials Chemistry* **20**, 5785 (2010).
- ¹² Y. Long, T. Saito, T. Tohyama, K. Oka, M. Azuma, and Y. Shimakawa, *Inorganic Chemistry* **48**, 8489 (2009).
- ¹³ Y. Long, T. Kawakami, W. Chen, T. Saito, T. Watanuki, Y. Nakakura, Q. Liu, C. Jin, and Y. Shimakawa, *Chem. Mater.* **24**, 2235 (2012).
- ¹⁴ A. Aimi, D. Mori, K. Hiraki, T. Takahashi, Y.J. Shan, Y. Shirako, J. Zhou, and Y. Inaguma, *Chem. Mater.* **26**, 2601 (2014).
- ¹⁵ J. Zhang and H. Li, *Perovskite: Crystallography, Chemistry and Catalytic Performance* (Nova Publishers, 2013).
- ¹⁶ J.L. García-Muñoz, J. Rodríguez-Carvajal, P. Lacorre, and J.B. Torrance, *Physical Review B* **46**, 4414 (1992).
- ¹⁷ G. Catalan, *Phase Transitions* **81**, 729 (2008).
- ¹⁸ N. Biškup, A. de Andrés, and M.G. Hernández, *Physical Review B* **78**, 184435 (2008).
- ¹⁹ A.M.L. Lopes, J.P. Araújo, V.S. Amaral, J.G. Correia, Y. Tomioka, and Y. Tokura, *Physical Review Letters* **100**, 155702 (2008).
- ²⁰ Z. Jirák, E. Hadová, O. Kaman, K. Knížek, M. Maryško, E. Pollert, M. Dlouhá, and S. Vratislav, *Physical Review B* **81**, 024403 (2010).
- ²¹ B. Padmanabhan, H.L. Bhat, S. Elizabeth, S. Röbber, U.K. Röbber, K. Dörr, and K.H. Müller, *Physical Review B* **75**, 024419 (2007).
- ²² T. Satoh, Y. Kikuchi, K. Miyano, E. Pollert, J. Hejtmánek, and Z. Jirák, *Physical Review B* **65**, 125103 (2002).
- ²³ Y. Uozu, Y. Wakabayashi, Y. Ogimoto, N. Takubo, H. Tamaru, N. Nagaosa, and K. Miyano, *Physical Review Letters* **97**, 037202 (2006).
- ²⁴ G. Colizzi, A. Filippetti, and V. Fiorentini, *Physical Review B* **82**, 140101 (2010).
- ²⁵ J. Fan, L. Pi, L. Zhang, W. Tong, L. Ling, B. Hong, Y. Shi, W. Zhang, D. Lu, and Y. Zhang, *Physica B: Condensed Matter* **406**, 2289 (2011).

- ²⁶ P. Balasubramanian, S.R. Joshi, R. Yadav, F.M. de Groot, A.K. Singh, A. Ray, M. Gupta, A. Singh, S. Maurya, and S. Elizabeth, *Journal of Physics: Condensed Matter* **30**, 435603 (2018).
- ²⁷ J. Hemberger, M. Brando, R. Wehn, V.Y. Ivanov, A.A. Mukhin, A.M. Balbashov, and A. Loidl, *Physical Review B* **69**, 064418 (2004).
- ²⁸ V. Dyakonov, F. Bukhanko, V. Kamenev, E. Zubov, S. Baran, T. Jaworska-Gołab, A. Szytuła, E. Wawrzyńska, B. Penc, and R. Duraj, *Physical Review B* **74**, 024418 (2006).
- ²⁹ J.A. Alonso, M.J. Martínez-Lope, M.T. Casais, and M.T. Fernández-Díaz, *Inorganic Chemistry* **39**, 917 (2000).
- ³⁰ M. Medarde, C. Dallera, M. Grioni, B. Delley, F. Vernay, J. Mesot, M. Sikora, J.A. Alonso, and M.J. Martínez-Lope, *Physical Review B* **80**, 245105 (2009).
- ³¹ S. Harisankar, K. Soni, and K.R. Mavani, *Materials Research Express* **6**, 116107 (2019).
- ³² P. Lacorre, J.B. Torrance, J. Pannetier, A.I. Nazzari, P.W. Wang, and T.C. Huang, *Journal of Solid State Chemistry* **91**, 225 (1991).
- ³³ X. Huang, L. Pei, Z. Liu, Z. Lu, Y. Sui, Z. Qian, and W. Su, *Journal of Alloys and Compounds* **345**, 265 (2002).
- ³⁴ L. Martin-Carron and A. De Andrés, *Physical Review Letters* **92**, 175501 (2004).
- ³⁵ M.N. Iliev, M.V. Abrashev, J. Laverdiere, S. Jandl, M.M. Gospodinov, Y.-Q. Wang, and Y.-Y. Sun, *Physical Review B* **73**, 064302 (2006).
- ³⁶ M.W. Kim, S.J. Moon, J.H. Jung, J. Yu, S. Parashar, P. Murugavel, J.H. Lee, and T.W. Noh, *Physical Review Letters* **96**, 247205 (2006).
- ³⁷ B. Levasseur and S. Kaliaguine, *Journal of Solid State Chemistry* **181**, 2953 (2008).
- ³⁸ B. Bouadjemi, S. Bentata, A. Abbad, W. Benstaali, and B. Bouhafs, *Solid State Communications* **168**, 6 (2013).
- ³⁹ R. Kováčik, S.S. Murthy, C.E. Quiroga, C. Ederer, and C. Franchini, *Physical Review B* **93**, 075139 (2016).
- ⁴⁰ S.K. Mishra, M.K. Gupta, R. Mittal, A.I. Kolesnikov, and S.L. Chaplot, *Physical Review B* **93**, 214306 (2016).
- ⁴¹ T. Mizokawa, A. Fujimori, T. Arima, Y. Tokura, N. Mōri, and J. Akimitsu, *Physical Review B* **52**, 13865 (1995).
- ⁴² G. Giovannetti, S. Kumar, D. Khomskii, S. Picozzi, and J. van den Brink, *Physical Review Letters* **103**, 156401 (2009).
- ⁴³ J. Varignon, M.N. Grisolia, J. Íñiguez, A. Barthélémy, and M. Bibes, *Npj Quantum Materials* **2**, 1 (2017).
- ⁴⁴ J. Bak, H.B. Bae, and S.-Y. Chung, *Nature Communications* **10**, 1 (2019).
- ⁴⁵ P.E. Marti and A. Baiker, *Catalysis Letters* **26**, 71 (1994).
- ⁴⁶ T. Ishihara, T. Kudo, H. Matsuda, and Y. Takita, *Journal of the Electrochemical Society* **142**, 1519 (1995).
- ⁴⁷ N. Biškup, A. De Andrés, J.L. Martínez, and C. Perca, *Physical Review B* **72**, 024115 (2005).
- ⁴⁸ R.S. Freitas, J.F. Mitchell, and P. Schiffer, *Physical Review B* **72**, 144429 (2005).
- ⁴⁹ S. Grenier, J.P. Hill, D. Gibbs, K.J. Thomas, M. v Zimmermann, C.S. Nelson, V. Kiryukhin, Y. Tokura, Y. Tomioka, and D. Casa, *Physical Review B* **69**, 134419 (2004).
- ⁵⁰ K.A. Resende, C.N. Ávila-Neto, R.C. Rabelo-Neto, F.B. Noronha, and C.E. Hori, *Catalysis Today* **242**, 71 (2015).
- ⁵¹ S. Das, G.L. Prajapati, P. Anagha, and D.S. Rana, *Physical Review B* **98**, 115110 (2018).
- ⁵² S. Singh and M. Rakesh, *J Inorg Organomet Polym* **27**, 1719 (2017).
- ⁵³ M. El Amine Monir and F.Z. Dahou, *SN Appl. Sci.* **2**, 465 (2020).
- ⁵⁴ R. Kumar, R.J. Choudhary, M. Ikram, D.K. Shukla, S. Mollah, P. Thakur, K.H. Chae, B. Angadi, and W.K. Choi, *Journal of Applied Physics* **102**, 073707 (2007).

- ⁵⁵ K. Kim, S. Joo, R. Huang, H.J. Kim, G. Kim, and J.W. Han, *Energy & Environmental Science* **14**, 873 (2021).
- ⁵⁶ S. Nair and A. Banerjee, *Physical Review Letters* **93**, 117204 (2004).
- ⁵⁷ K. Yoshimatsu, H. Wadati, E. Sakai, T. Harada, Y. Takahashi, T. Harano, G. Shibata, K. Ishigami, T. Kadono, and T. Koide, *Physical Review B* **88**, 174423 (2013).
- ⁵⁸ R. M'nassri, A. Selmi, N.C. Boudjada, and A. Cheikhrouhou, *Journal of Thermal Analysis and Calorimetry* **129**, 53 (2017).
- ⁵⁹ Z.W. Ouyang, H. Nojiri, and S. Yoshii, *Physical Review B* **78**, 104404 (2008).
- ⁶⁰ R. Cherif, E.K. Hlil, M. Ellouze, F. Elhalouani, and S. Obbade, *Journal of Materials Science* **49**, 8244 (2014).
- ⁶¹ H. Nakatsugawa, M. Saito, and Y. Okamoto, *Journal of Electronic Materials* **46**, 3262 (2017).
- ⁶² G.C. Kostoglou and C. Ftikos, *Solid State Ionics* **109**, 43 (1998).
- ⁶³ R.I. Dass and J.B. Goodenough, *Physical Review B* **67**, 014401 (2003).
- ⁶⁴ P. Padhan, H.Z. Guo, P. LeClair, and A. Gupta, *Applied Physics Letters* **92**, 022909 (2008).
- ⁶⁵ K. Zhang, L. Ge, R. Ran, Z. Shao, and S. Liu, *Acta Materialia* **56**, 4876 (2008).
- ⁶⁶ M.T. Anderson, K.B. Greenwood, G.A. Taylor, and K.R. Poeppelmeier, *Progress in Solid State Chemistry* **22**, 197 (1993).
- ⁶⁷ S.J. Mugavero III, A.H. Fox, M.D. Smith, and H.-C. zur Loye, *Journal of Solid State Chemistry* **183**, 465 (2010).
- ⁶⁸ S.J. Makowski, J.A. Rodgers, P.F. Henry, J.P. Attfield, and J.-W.G. Bos, *Chemistry of Materials* **21**, 264 (2009).
- ⁶⁹ W.R. Gemmill, M.D. Smith, and H.-C. zur Loye, *Journal of Solid State Chemistry* **179**, 1750 (2006).
- ⁷⁰ M.J. Davis, S.J. Mugavero III, K.I. Glab, M.D. Smith, and H.-C. zur Loye, *Solid State Sciences* **6**, 413 (2004).
- ⁷¹ X. Chen, J. Xu, Y. Xu, F. Luo, and Y. Du, *Inorganic Chemistry Frontiers* **6**, 2226 (2019).
- ⁷² W.R. Gemmill, M.D. Smith, R. Prozorov, and H.-C. zur Loye, *Inorganic Chemistry* **44**, 2639 (2005).
- ⁷³ W.R. Gemmill, M.D. Smith, and H.-C. zur Loye, *Journal of Solid State Chemistry* **177**, 3560 (2004).
- ⁷⁴ M.T. Haque and N. Kamegashira, *Journal of Alloys and Compounds* **395**, 220 (2005).
- ⁷⁵ N. Kamegashira, M. Kobayashi, and J.-I. Saito, in *Frontiers of Solid State Chemistry* (WORLD SCIENTIFIC, 2002), pp. 47–52.
- ⁷⁶ I.N. Bhatti, I.N. Bhatti, R.N. Mahato, and M.A.H. Ahsan, *Physics Letters A* **383**, 2326 (2019).
- ⁷⁷ C. Xie, L. Shi, J. Zhao, S. Zhou, Y. Li, and X. Yuan, *Journal of Applied Physics* **120**, 155302 (2016).
- ⁷⁸ H.J. Zhao, H. Zhou, X.M. Chen, and L. Bellaiche, *Journal of Physics: Condensed Matter* **27**, 226001 (2015).
- ⁷⁹ L.Y. Wang, Q. Li, Y.Y. Gong, D.H. Wang, Q.Q. Cao, and Y.W. Du, *Journal of the American Ceramic Society* **97**, 2024 (2014).
- ⁸⁰ K. Aswathi, J.P. Palakkal, P.N. Lekshmi, and M.R. Varma, *New Journal of Chemistry* **43**, 17351 (2019).
- ⁸¹ Y. Jia, Y. Cheng, H. Wang, Z. Zhang, and L. Li, *Ceramics International* **46**, 25043 (2020).
- ⁸² E. Solana-Madruga, Á.M. Arévalo-López, A.J. Dos santos-García, C. Ritter, C. Cascales, R. Sáez-Puche, and J.P. Attfield, *Physical Review B* **97**, 134408 (2018).
- ⁸³ M. Azuma, S. Kaimori, and M. Takano, *Chemistry of Materials* **10**, 3124 (1998).
- ⁸⁴ D.K. Mahato and T.P. Sinha, *Journal of Electronic Materials* **46**, 107 (2017).

- ⁸⁵ K. Ouchetto, F. Archaimbault, J. Choisnet, and M. Et-Tabirou, *Materials Chemistry and Physics* **51**, 117 (1997).
- ⁸⁶ T. Ferreira, G. Morrison, J. Yeon, and H.-C. zur Loye, *Crystal Growth & Design* **16**, 2795 (2016).
- ⁸⁷ K.D. Truong, M.P. Singh, S. Jandl, and P. Fournier, *Journal of Physics: Condensed Matter* **23**, 052202 (2011).
- ⁸⁸ Y. Zhang, H. Li, D. Guo, L. Hou, X. Li, Z. Ren, and G. Wilde, *Ceramics International* **44**, 20762 (2018).
- ⁸⁹ D.K. Mahato, M. Rudra, and T.P. Sinha, *Journal of Alloys and Compounds* **689**, 617 (2016).
- ⁹⁰ T. Kawano, J. Takahashi, T. Yamada, and H. Yamane, *Journal of the Ceramic Society of Japan* **115**, 792 (2007).
- ⁹¹ N. Das, M.A. Nath, G.S. Thakur, M. Thirumal, and A.K. Ganguli, *Journal of Solid State Chemistry* **229**, 97 (2015).
- ⁹² D.K. Mahato and T.P. Sinha, *Journal of Materials Science: Materials in Electronics* **24**, 4399 (2013).
- ⁹³ S. Ravi, *Journal of Rare Earths* **36**, 1175 (2018).
- ⁹⁴ N. Das, S. Singh, A.G. Joshi, M. Thirumal, V.R. Reddy, L.C. Gupta, and A.K. Ganguli, *Inorg. Chem.* **56**, 12712 (2017).
- ⁹⁵ J. Kanamori, *Journal of Physics and Chemistry of Solids* **10**, 87 (1959).
- ⁹⁶ J.B. Goodenough, *Physical Review* **100**, 564 (1955).
- ⁹⁷ R.I. Dass, J.-Q. Yan, and J.B. Goodenough, *Physical Review B* **68**, 064415 (2003).
- ⁹⁸ A. Venimadhav, D. Chandrasekar, and J.K. Murthy, *Applied Nanoscience* **3**, 25 (2013).
- ⁹⁹ A.J. Millis, *Nature* **392**, 147 (1998).
- ¹⁰⁰ H. Röder, J. Zang, and A.R. Bishop, *Physical Review Letters* **76**, 1356 (1996).
- ¹⁰¹ J. Zang, A.R. Bishop, and H. Röder, *Physical Review B* **53**, R8840 (1996).
- ¹⁰² J.-M. Tarascon, W.R. McKinnon, L.H. Greene, G.W. Hull, Vogel, and EM, *Physical Review B* **36**, 226 (1987).
- ¹⁰³ R.J. Cava, B. Batlogg, J.J. Krajewski, R. Farrow, L.J. Rupp, A.E. White, K. Short, W.F. Peck, and T. Kometani, *Nature* **332**, 814 (1988).
- ¹⁰⁴ H. Tanaka and M. Misono, *Current Opinion in Solid State and Materials Science* **5**, 381 (2001).
- ¹⁰⁵ R. Mohassel, A. Sobhani, and M. Salavati-Niasari, *International Journal of Hydrogen Energy* **44**, 860 (2019).
- ¹⁰⁶ R. Hu, R. Ding, J. Chen, J. Hu, and Y. Zhang, *Catalysis Communications* **21**, 38 (2012).
- ¹⁰⁷ Y. Shimakawa, M. Azuma, and N. Ichikawa, *Materials* **4**, 153 (2011).
- ¹⁰⁸ S. Arif and A. Faraz, *Journal of Electronic Materials* **48**, 7515 (2019).
- ¹⁰⁹ W. Prellier, M.P. Singh, and P. Murugavel, *J. Phys.: Condens. Matter* **17**, R803 (2005).
- ¹¹⁰ R.B. Macedo Filho, D.A.B. Barbosa, H. Reichlova, X. Marti, A.S. De Menezes, A.P. Ayala, and C.W.A. Paschoal, *Materials Research Express* **2**, 075201 (2015).
- ¹¹¹ R. Ramesh and N.A. Spaldin, *Nanoscience And Technology: A Collection of Reviews from Nature Journals* **20** (2010).
- ¹¹² W. Eerenstein, N.D. Mathur, and J.F. Scott, *Nature* **442**, 759 (2006).
- ¹¹³ H.Z. Guo, J. Burgess, E. Ada, S. Street, A. Gupta, M.N. Iliev, A.J. Kellock, C. Magen, M. Varela, and S.J. Pennycook, *Physical Review B* **77**, 174423 (2008).
- ¹¹⁴ K. Shigematsu, A. Chikamatsu, T. Fukumura, S. Toyoda, E. Ikenaga, and T. Hasegawa, *Appl. Phys. Lett.* **104**, 261901 (2014).
- ¹¹⁵ M.C. Sánchez, J. García, J. Blasco, G. Subías, and J. Perez-Cacho, *Physical Review B* **65**, 144409 (2002).
- ¹¹⁶ M. Sonobe and K. Asai, *Journal of the Physical Society of Japan* **61**, 4193 (1992).

- ¹¹⁷ J.-S. Kang, S.M. Lee, D.H. Kim, S. Kolesnik, B. Dabrowski, B.-G. Park, J.-Y. Kim, J. Lee, B. Kim, and B.I. Min, *Journal of Applied Physics* **107**, 09D721 (2010).
- ¹¹⁸ I.O. Troyanchuk, N.V. Samsonenko, E.F. Shapovalova, H. Szymczak, and A. Nabialek, *Materials Research Bulletin* **32**, 67 (1997).
- ¹¹⁹ M. Mouallem-Bahout, T. Roisnel, F. Bourée, G. André, C. Moure, and O. Peña, *Progress in Solid State Chemistry* **35**, 257 (2007).
- ¹²⁰ C.L. Bull and P.F. McMillan, *Journal of Solid State Chemistry* **177**, 2323 (2004).
- ¹²¹ M. Nasir, S. Kumar, N. Patra, D. Bhattacharya, S.N. Jha, D.R. Basaula, S. Bhatt, M. Khan, S.-W. Liu, and S. Biring, *ACS Applied Electronic Materials* **1**, 141 (2019).
- ¹²² R.J. Booth, R. Fillman, H. Whitaker, A. Nag, R.M. Tiwari, K.V. Ramanujachary, J. Gopalakrishnan, and S.E. Lofland, *Materials Research Bulletin* **44**, 1559 (2009).
- ¹²³ M. Kumar, B. Prajapati, and A. Singh, *J Mater Sci: Mater Electron* **31**, 8099 (2020).
- ¹²⁴ M. Kumar, B. Prajapati, A. Singh, S. Kumar, A. Kumar, S. Mittal, and Aditya, *Chemical Physics* **532**, 110688 (2020).
- ¹²⁵ T. Wang, H.-Y. Wu, Y.-B. Sun, R. Xing, B. Xv, and J.-J. Zhao, *J Supercond Nov Magn* **33**, 727 (2020).
- ¹²⁶ H. Gan, J. Shi, C. Wang, and Q. Shen, *Applied Surface Science* **561**, 150102 (2021).
- ¹²⁷ H. Gan, C. Wang, and Q. Shen, *Ceramics International* **46**, 8995 (2020).
- ¹²⁸ S.A.U. Islam, K. Sultan, S.A. Bhat, N. Nazir, and M. Ikram, *SN Appl. Sci.* **2**, 728 (2020).
- ¹²⁹ N. Brahiti, M. Abbasi Eskandari, M. Balli, C. Gauvin-Ndiaye, R. Nourafkan, A.-M.S. Tremblay, and P. Fournier, *Journal of Applied Physics* **127**, 113905 (2020).
- ¹³⁰ S. Kumar, G. Giovannetti, J. van den Brink, and S. Picozzi, *Physical Review B* **82**, 134429 (2010).
- ¹³¹ J.B. de Azevedo Filho, R.F. Souza, J.C.A. Queiroz, T.H.C. Costa, C.P.S. Sena, S.G.C. Fonseca, A.O. da Silva, and J.B.L. Oliveira, *Journal of Magnetism and Magnetic Materials* **527**, 167770 (2021).
- ¹³² M. Kumar, B. Prajapati, A. Raj, A. Anshul, P. Chandra Sati, M. Sahni, and A. Kumar, *Materials Today: Proceedings* (2020).
- ¹³³ H.J. Zhao, W. Ren, Y. Yang, J. Íñiguez, X.M. Chen, and L. Bellaiche, *Nature Communications* **5**, 1 (2014).
- ¹³⁴ A.K. Singh, S. Chauhan, P. Balasubramanian, S.K. Srivastava, and R. Chandra, *Thin Solid Films* **629**, 49 (2017).
- ¹³⁵ S. Pal, S. Jana, S. Govinda, B. Pal, S. Mukherjee, S. Keshavarz, D. Thonig, Y. Kvashnin, M. Pereiro, and R. Mathieu, *Physical Review B* **100**, 045122 (2019).
- ¹³⁶ R. Das and R.N.P. Choudhary, *Journal of Advanced Ceramics* **8**, 174 (2019).
- ¹³⁷ M.S. Sheikh, A.P. Sakhya, R. Maity, A. Dutta, and T.P. Sinha, *Solar Energy Materials and Solar Cells* **193**, 206 (2019).
- ¹³⁸ I.P. Kokila, P.S. Kumar, M. Kanagaraj, A.K. Paidi, L. He, S. Madeswaran, and H.A. Therese, *Journal of Nanoparticle Research* **22**, 1 (2020).
- ¹³⁹ M.S. Sheikh, A.P. Sakhya, A. Dutta, and T.P. Sinha, *Computational Materials Science* **161**, 293 (2019).
- ¹⁴⁰ L. Su, X.-Q. Zhang, Q.-Y. Dong, Y.-J. Ke, K.-Y. Hou, C.-S. Liu, and Z.-H. Cheng, *Journal of Alloys and Compounds* **746**, 594 (2018).
- ¹⁴¹ M.S. Sheikh, D. Ghosh, A. Dutta, S. Bhattacharyya, and T.P. Sinha, *Materials Science and Engineering: B* **226**, 10 (2017).
- ¹⁴² A. Kumar, A. Kumar, and A. Kumar, *Solid State Sciences* **105**, 106252 (2020).
- ¹⁴³ A. Tripathy, S.N. Das, S. Bhuyan, and R.N.P. Choudhary, *Materials Today: Proceedings* **35**, 109 (2021).
- ¹⁴⁴ N. Nazir and M. Ikram, *Journal of Materials Science: Materials in Electronics* **31**, 23002 (2020).

- ¹⁴⁵ H. Nhalil, H.S. Nair, H.L. Bhat, and S. Elizabeth, *EPL (Europhysics Letters)* **104**, 67002 (2014).
- ¹⁴⁶ H.S. Nair, D. Swain, S. Adiga, C. Narayana, and S. Elizabeth, *Journal of Applied Physics* **110**, 123919 (2011).
- ¹⁴⁷ J. Singh, I. Rogge, U.K. Goutam, and A. Kumar, *Ionics* **26**, 5143 (2020).
- ¹⁴⁸ L. Wu, L. Shi, X. Miao, S. Zhou, J. Zhao, S. Pan, J. Guo, and X. Yuan, *Physica Status Solidi (b)* **256**, 1900168 (2019).
- ¹⁴⁹ R. Das and R.N.P. Choudhary, *Solid State Sciences* **87**, 1 (2019).
- ¹⁵⁰ M.S. Sheikh, S. Chanda, A. Dey, A. Dutta, P.P. Ray, and T.P. Sinha, *Ferroelectrics* **518**, 204 (2017).
- ¹⁵¹ M.G. Masud, K. Dey, A. Ghosh, S. Majumdar, and S. Giri, *Journal of Applied Physics* **118**, 064104 (2015).
- ¹⁵² T. Chakraborty, H. Nhalil, R. Yadav, A.A. Wagh, and S. Elizabeth, *Journal of Magnetism and Magnetic Materials* **428**, 59 (2017).
- ¹⁵³ Y. Jia, Q. Wang, Y. Qi, and L. Li, *Journal of Alloys and Compounds* **726**, 1132 (2017).
- ¹⁵⁴ H. Lu, X. Sun, Z. Hou, W. Yang, S. Wang, J. Xie, and L. Deng, *AIP Advances* **6**, 035219 (2016).
- ¹⁵⁵ M. Retuerto, A. Munoz, M.J. Martínez-Lope, J.A. Alonso, F.J. Mompean, M.T. Fernandez-Diaz, and J. Sanchez-Benitez, *Inorganic Chemistry* **54**, 10890 (2015).
- ¹⁵⁶ K. Manna, A.K. Bera, M. Jain, S. Elizabeth, S.M. Yusuf, and P.A. Kumar, *Physical Review B* **91**, 224420 (2015).
- ¹⁵⁷ S. Chanda, S. Saha, A. Dutta, J. Krishna Murthy, A. Venimadhav, S. Shannigrahi, and T.P. Sinha, *Journal of Applied Physics* **120**, 134102 (2016).
- ¹⁵⁸ L. Zhang, T.L. Shi, J.J. Cao, S.M. Yan, Y. Fang, Z.D. Han, B. Qian, X.F. Jiang, and D.H. Wang, *Journal of Alloys and Compounds* **763**, 613 (2018).
- ¹⁵⁹ C. Zhang, W. Zhu, L. Yuan, and H. Yuan, *Journal of Alloys and Compounds* **744**, 395 (2018).
- ¹⁶⁰ A.V. Sobolev, I.S. Glazkova, A.A. Akulenko, I. Sergueev, A.I. Chumakov, W. Yi, A.A. Belik, and I.A. Presniakov, *The Journal of Physical Chemistry C* **123**, 23628 (2019).
- ¹⁶¹ C. Xie and L. Shi, *Applied Surface Science* **384**, 459 (2016).
- ¹⁶² M. Alam, K. Mandal, and G.G. Khan, *Journal of Alloys and Compounds* **822**, 153540 (2020).
- ¹⁶³ L. Shen, Z. Meng, W. Liu, X. Xu, T. Sun, Y. Liu, W. Zhu, H. Huang, R. Zhang, and S. Zhang, *Journal of Magnetism and Magnetic Materials* **519**, 167427 (2021).
- ¹⁶⁴ G. Blasse, *Journal of Physics and Chemistry of Solids* **26**, 1969 (1965).
- ¹⁶⁵ G.H. Jonker, *Physica* **22**, 707 (1956).
- ¹⁶⁶ H. Lin, X.X. Shi, and X.M. Chen, *Journal of Alloys and Compounds* **709**, 772 (2017).
- ¹⁶⁷ P.N. Lekshmi, M. Vasundhara, M.R. Varma, K.G. Suresh, and M. Valant, *Physica B: Condensed Matter* **448**, 285 (2014).
- ¹⁶⁸ H. Li, L.-P. Sun, Q. Li, T. Xia, H. Zhao, L.-H. Huo, J.-M. Bassat, A. Rougier, S. Fourcade, and J.-C. Grenier, *International Journal of Hydrogen Energy* **40**, 12761 (2015).
- ¹⁶⁹ L. Sun, H. Li, J. Zhao, G. Wang, L. Huo, and H. Zhao, *Journal of Alloys and Compounds* **777**, 1319 (2019).
- ¹⁷⁰ D. Tiana, C.H. Hendon, and A. Walsh, *Chemical Communications* **50**, 13990 (2014).
- ¹⁷¹ T. Saha-Dasgupta, *Journal of Superconductivity and Novel Magnetism* **26**, 1991 (2013).
- ¹⁷² D.J. Singh and C.H. Park, *Physical Review Letters* **100**, 087601 (2008).
- ¹⁷³ H. Das, U.V. Waghmare, T. Saha-Dasgupta, and D.D. Sarma, *Physical Review Letters* **100**, 186402 (2008).
- ¹⁷⁴ C. Shi, Y. Hao, and Z. Hu, *Journal of Physics D: Applied Physics* **44**, 245405 (2011).
- ¹⁷⁵ M.P. Singh, K.D. Truong, S. Jandl, and P. Fournier, *Journal of Applied Physics* **107**,

09D917 (2010).

¹⁷⁶ H.J. Zhao, X.Q. Liu, X.M. Chen, and L. Bellaiche, *Physical Review B* **90**, 195147 (2014).

¹⁷⁷ D.C. Kakarla, K.M. Jyothinagaram, A.K. Das, and V. Adyam, *Journal of the American Ceramic Society* **97**, 2858 (2014).

¹⁷⁸ J.B. Goodenough, *Reports on Progress in Physics* **67**, 1915 (2004).

¹⁷⁹ K. Asai, K. Fujiyoshi, N. Nishimori, Y. Satoh, Y. Kobayashi, and M. Mizoguchi, *Journal of the Physical Society of Japan* **67**, 4218 (1998).

¹⁸⁰ R.D. Shannon, *Acta Crystallographica Section A: Crystal Physics, Diffraction, Theoretical and General Crystallography* **32**, 751 (1976).

¹⁸¹ K. Asai, N. Kobayashi, T. Bairo, N. Kaneko, Y. Kobayashi, M. Suzuki, Y. Satoh, and M. Mizoguchi, *Journal of the Physical Society of Japan* **74**, 1289 (2005).

¹⁸² W.Z. Yang, X.Q. Liu, H.J. Zhao, Y.Q. Lin, and X.M. Chen, *Journal of Applied Physics* **112**, 064104 (2012).

¹⁸³ D. Louca and T. Egami, *Physical Review B* **59**, 6193 (1999).

¹⁸⁴ V. Cuartero, S. Lafuerza, M. Rovezzi, J. García, J. Blasco, G. Subías, and E. Jiménez, *Physical Review B* **94**, 155117 (2016).

¹⁸⁵ J. Su, Z.Z. Yang, X.M. Lu, J.T. Zhang, L. Gu, C.J. Lu, Q.C. Li, J.-M. Liu, and J.S. Zhu, *ACS Applied Materials & Interfaces* **7**, 13260 (2015).

¹⁸⁶ G. Zhang, G. Li, F. Liao, Y. Fu, M. Xiong, and J. Lin, *Journal of Crystal Growth* **327**, 262 (2011).

¹⁸⁷ A. Ali, G. Sharma, A. Vardhan, K. Pasrija, S. Rajput, T. Maitra, S. Kumar, and Y. Singh, *Journal of Physics: Condensed Matter* **31**, 305803 (2019).

¹⁸⁸ A. Ali, K. Pasrija, G. Sharma, S. Kumar, and Y. Singh, *ArXiv Preprint ArXiv:2105.12331* (2021).

¹⁸⁹ T. Asaka, X.Z. Yu, Y. Tomioka, Y. Kaneko, T. Nagai, K. Kimoto, K. Ishizuka, Y. Tokura, and Y. Matsui, *Physical Review B* **75**, 184440 (2007).

¹⁹⁰ A. Hossain, A.A. Ullah, P.S. Guin, and S. Roy, *Journal of Sol-Gel Science and Technology* **93**, 479 (2020).

¹⁹¹ R. Yadav and S. Elizabeth, *Journal of Applied Physics* **117**, 053902 (2015).

¹⁹² J.K. Murthy, K.D. Chandrasekhar, S. Mahana, D. Topwal, and A. Venimadhav, *Journal of Physics D: Applied Physics* **48**, 355001 (2015).

¹⁹³ S.H. Oh, H.Y. Choi, J.Y. Moon, M.K. Kim, Y. Jo, N. Lee, and Y.J. Choi, *Journal of Physics D: Applied Physics* **48**, 445001 (2015).

¹⁹⁴ T. Chakraborty, H.S. Nair, H. Nhalil, K.R. Kumar, A.M. Strydom, and S. Elizabeth, *Journal of Physics: Condensed Matter* **29**, 025804 (2016).

¹⁹⁵ A. Kaippamagalath, J.P. Palakkal, A.P. Paulose, and M.R. Varma, *Ferroelectrics* **518**, 223 (2017).

¹⁹⁶ W.-J. Yin, B. Weng, J. Ge, Q. Sun, Z. Li, and Y. Yan, *Energy & Environmental Science* **12**, 442 (2019).

¹⁹⁷ V.J. Joly, P.A. Joy, S.K. Date, and C.S. Gopinath, *Physical Review B* **65**, 184416 (2002).

¹⁹⁸ L. Sun, H. Li, J. Zhao, G. Wang, L. Huo, and H. Zhao, *Journal of Alloys and Compounds* **777**, 1319 (2019).

¹⁹⁹ M.P. Singh, K.D. Truong, S. Jandl, and P. Fournier, *Applied Physics Letters* **98**, 162506 (2011).

²⁰⁰ G. Zhang, G. Li, F. Liao, Y. Fu, M. Xiong, and J. Lin, *Journal of Crystal Growth* **327**, 262 (2011).

²⁰¹ F.N. Sayed, S.N. Achary, O.D. Jayakumar, S.K. Deshpande, P.S.R. Krishna, S. Chatterjee, P. Ayyub, and A.K. Tyagi, *Journal of Materials Research* **26**, 567 (2011).

²⁰² S.N. Achary, V. Katari, F.N. Sayed, and A.K. Tyagi, *Journal of Chemical Sciences* **131**, 1 (2019).

- ²⁰³ P.J. Saines, (2008).
- ²⁰⁴ C.J. Howard and M.A. Carpenter, *Acta Crystallographica Section B: Structural Science* **66**, 40 (2010).
- ²⁰⁵ A.M. Glazer, *Acta Crystallographica Section A* **31**, 756 (1975).
- ²⁰⁶ B. Manoun, J.M. Igartua, and P. Lazor, *Journal of Molecular Structure* **971**, 18 (2010).
- ²⁰⁷ E.G. Rini, A. Paul, M. Nasir, R. Amin, M.K. Gupta, R. Mittal, and S. Sen, *Journal of Alloys and Compounds* **830**, 154594 (2020).
- ²⁰⁸ C. Meneghini, S. Ray, F. Liscio, F. Bardelli, S. Mobilio, and D.D. Sarma, *Physical Review Letters* **103**, 046403 (2009).
- ²⁰⁹ I.R. De Larramendi, N. Ortiz-Vitoriano, B. Acebedo, D.J. De Aberasturi, I.G. De Muro, A. Arango, E. Rodríguez-Castellón, J.I.R. De Larramendi, and T. Rojo, *International Journal of Hydrogen Energy* **36**, 10981 (2011).
- ²¹⁰ A.T. Fulmer, J. Dondlinger, and M.A. Langell, *Applied Surface Science* **305**, 544 (2014).
- ²¹¹ K. Asai, H. Sekizawa, and S. Iida, *Journal of the Physical Society of Japan* **47**, 1054 (1979).
- ²¹² M.N. Iliev, M.V. Abrashev, H.-G. Lee, V.N. Popov, Y.Y. Sun, C. Thomsen, R.L. Meng, and C.W. Chu, *Physical Review B* **57**, 2872 (1998).
- ²¹³ M.N. Iliev, M.V. Abrashev, A.P. Litvinchuk, V.G. Hadjiev, H. Guo, and A. Gupta, *Physical Review B* **75**, 104118 (2007).
- ²¹⁴ S.B. Ogale, T.V. Venkatesan, and M. Blamire, *Functional Metal Oxides: New Science and Novel Applications* (John Wiley & Sons, 2013).
- ²¹⁵ M.N. Iliev, H. Guo, and A. Gupta, *Applied Physics Letters* **90**, 151914 (2007).
- ²¹⁶ K.D. Truong, J. Laverdière, M.P. Singh, S. Jandl, and P. Fournier, *Physical Review B* **76**, 132413 (2007).
- ²¹⁷ C. Meyer, P. Ksoll, V. Roddatis, and V. Moshnyaga, *Crystals* **11**, 747 (2021).
- ²¹⁸ K.D. Truong, M.P. Singh, S. Jandl, and P. Fournier, *Physical Review B* **80**, 134424 (2009).
- ²¹⁹ D. Kumar, S. Kumar, and V.G. Sathe, *Solid State Communications* **194**, 59 (2014).
- ²²⁰ C. Meyer, S. Hühn, M. Jungbauer, S. Merten, B. Damaschke, K. Samwer, and V. Moshnyaga, *Journal of Raman Spectroscopy* **48**, 46 (2017).
- ²²¹ J.-C. Panitz, J.-C. Mayor, B. Grob, and W. Durisch, *Journal of Alloys and Compounds* **303**, 340 (2000).
- ²²² M. Balkanski, R.F. Wallis, and E. Haro, *Physical Review B* **28**, 1928 (1983).
- ²²³ E. Granado, A. García, J.A. Sanjurjo, C. Rettori, I. Torriani, F. Prado, R.D. Sánchez, A. Caneiro, and S.B. Oseroff, *Physical Review B* **60**, 11879 (1999).
- ²²⁴ R.X. Silva, H. Reichlova, X. Marti, D.A.B. Barbosa, M.W. Lufaso, B.S. Araujo, A.P. Ayala, and C.W.A. Paschoal, *Journal of Applied Physics* **114**, 194102 (2013).
- ²²⁵ X.-W. Jin, L. Lu, S.-B. Mi, M. Liu, and C.-L. Jia, *Applied Physics Letters* **109**, 031904 (2016).
- ²²⁶ J. Laverdière, S. Jandl, A.A. Mukhin, V.Y. Ivanov, V.G. Ivanov, and M.N. Iliev, *Physical Review B* **73**, 214301 (2006).
- ²²⁷ M.N. Iliev, M.M. Gospodinov, M.P. Singh, J. Meen, K.D. Truong, P. Fournier, and S. Jandl, *Journal of Applied Physics* **106**, 023515 (2009).
- ²²⁸ H. Lueken, 92 (n.d.).
- ²²⁹ P.N. Lekshmi, G.R. Raji, M. Vasundhara, M.R. Varma, S.S. Pillai, and M. Valant, *J. Mater. Chem. C* **1**, 6565 (2013).
- ²³⁰ D.J. Newman and B. Ng, *Crystal Field Handbook* (Cambridge University Press, 2007).
- ²³¹ R. Das, P. Yanda, A. Sundaresan, and D.D. Sarma, *Materials Research Express* **6**, 116122 (2019).
- ²³² C. Ritter, M.R. Ibarra, L. Morellon, J. Blasco, J. Garcia, and J.M. De Teresa, *Journal of*

Physics: Condensed Matter **12**, 8295 (2000).

²³³ K.R. Chakraborty, A. Das, P.S.R. Krishna, S.M. Yusuf, S.J. Patwe, S.N. Achary, and A.K. Tyagi, *Journal of Alloys and Compounds* **457**, 15 (2008).

²³⁴ B.C. Tofield and W.R. Scott, *Journal of Solid State Chemistry* **10**, 183 (1974).

²³⁵ D. Haskel, G. Fabbri, N.M. Souza-Neto, M. Van Veenendaal, G. Shen, A.E. Smith, and M.A. Subramanian, *Physical Review B* **84**, 100403 (2011).

²³⁶ D.E. Cox and A.W. Sleight, *Acta Crystallographica Section B: Structural Crystallography and Crystal Chemistry* **35**, 1 (1979).

²³⁷ O. Chmaissem, R. Kruk, B. Dabrowski, D.E. Brown, X. Xiong, S. Kolesnik, J.D. Jorgensen, and C.W. Kimball, *Physical Review B* **62**, 14197 (2000).

²³⁸ A Gupta, G.Q. Gong, G. Xiao, P.R. Duncombe, P. Lecoeur, P. Trouilloud, Y.Y. Wang, V.P. Dravid, and J.Z. Sun, *Physical Review B* **54**, R15629 (1996).

²³⁹ T. Kyômen, R. Yamazaki, and M. Itoh, *Physical Review B* **68**, 104416 (2003).

²⁴⁰ J.H. Jung, K.H. Kim, D.J. Eom, T.W. Noh, E.J. Choi, J. Yu, Y.S. Kwon, and Y. Chung, *Physical Review B* **55**, 15489 (1997).

²⁴¹ R.J. Cava, *Journal of Materials Chemistry* **11**, 54 (2001).

²⁴² C.G. Koops, *Physical Review* **83**, 121 (1951).

²⁴³ J. Zaanen, G.A. Sawatzky, and J.W. Allen, *Physical Review Letters* **55**, 418 (1985).

²⁴⁴ H. Lu, X. Sun, Z. Hou, C. Dong, and L. Deng, *IEEE Transactions on Magnetics* **51**, 1 (2015).

²⁴⁵ B.K. Banerjee, *Physics Letters* **12**, 16 (1964).

²⁴⁶ A. Arrott and J.E. Noakes, *Phys. Rev. Lett.* **19**, 786 (1967).

²⁴⁷ L.-W. Li, *Chinese Phys. B* **25**, 037502 (2016).

²⁴⁸ Y. Zhang, *Journal of Alloys and Compounds* **787**, 1173 (2019).

²⁴⁹ D. Guo, H. Li, and Y. Zhang, *IEEE Trans. Magn.* **55**, 1 (2019).

²⁵⁰ L. Li, C. Xu, Y. Yuan, and S. Zhou, *Materials Research Letters* **6**, 413 (2018).

²⁵¹ L. Li, Y. Yuan, Y. Qi, Q. Wang, and S. Zhou, *Materials Research Letters* **6**, 67 (2018).

²⁵² Y. Zhang, H. Li, J. Wang, X. Li, Z. Ren, and G. Wilde, *Ceramics International* **44**, 1991 (2018).

²⁵³ Y. Zhang, H. Li, S. Geng, X. Lu, and G. Wilde, *Journal of Alloys and Compounds* **770**, 849 (2019).

²⁵⁴ K. Dey, A. Indra, S. Majumdar, and S. Giri, *Journal of Magnetism and Magnetic Materials* **435**, 15 (2017).

²⁵⁵ H.E. Stanley, *Rev. Mod. Phys.* **71**, S358 (1999).

²⁵⁶ S.N. Kaul, *Journal of Magnetism and Magnetic Materials* **53**, 5 (1985).

²⁵⁷ S.F. Fischer, S.N. Kaul, and H. Kronmüller, *Phys. Rev. B* **65**, 064443 (2002).

²⁵⁸ M. Balli, P. Fournier, S. Jandl, and M.M. Gospodinov, *Journal of Applied Physics* **115**, 173904 (2014).

²⁵⁹ D. Matte, M. de Lafontaine, A. Ouellet, M. Balli, and P. Fournier, *Phys. Rev. Applied* **9**, 054042 (2018).

²⁶⁰ J.K. Murthy, K.D. Chandrasekhar, S. Mahana, D. Topwal, and A. Venimadhav, *J. Phys. D: Appl. Phys.* **48**, 355001 (2015).

²⁶¹ Y. Jia, Q. Wang, Y. Qi, and L. Li, *Journal of Alloys and Compounds* **726**, 1132 (2017).

²⁶² Y. Jia, Q. Wang, P. Wang, and L. Li, *Ceramics International* **43**, 15856 (2017).

²⁶³ G. Sharma, T.S. Tripathi, J. Saha, and S. Patnaik, *Journal of Magnetism and Magnetic Materials* **368**, 318 (2014).

²⁶⁴ X. Luo, B. Wang, Y.P. Sun, X.B. Zhu, and W.H. Song, *J. Phys.: Condens. Matter* **20**, 465211 (2008).

²⁶⁵ K.L. Pan, G.T. Pan, S. Chong, and M.B. Chang, *Journal of Environmental Sciences* **69**, 205 (2018).

- ²⁶⁶ B.G. Shen, J.R. Sun, F.X. Hu, H.W. Zhang, and Z.H. Cheng, *Advanced Materials* **21**, 4545 (2009).
- ²⁶⁷ (n.d.).
- ²⁶⁸ Z.-Y. Wu, C.-B. Ma, X.-G. Tang, R. Li, Q.-X. Liu, and B.-T. Chen, *Nanoscale Research Letters* **8**, 207 (2013).
- ²⁶⁹ A.K. Biswal, J. Ray, S. Kuila, and P.N. Vishwakarma, *AIP Conference Proceedings* **1665**, 140050 (2015).
- ²⁷⁰ L.E. Cross, *Ferroelectrics* **76**, 241 (1987).